]REPORT DOCUMENTATION PAGE

AFRL-SR-BL-TR-01-

0225

1. AGENCY USE ONLY (Leave blank)	2. REPORT DATE	3. REPORT TYPE AND DATES COVERED	
4. TITLE AND SUBTITLE Development of Micro-Resolution PIV and Analysis of Microthrusters for Small Scale Aircraft and Spacecraft		**5. FUNDING NUMBERS** 8-442550-25381	
6. AUTHOR(S) Professor Carl D. Meinhart			
7. PERFORMING ORGANIZATION NAME(S) AND ADDRESS(ES) AFOSR/NA 110 Duncan Avenue Roon B115 Bolling AFB DC 20332-8050		**8. PERFORMING ORGANIZATION REPORT NUMBER**	
9. SPONSORING / MONITORING AGENCY NAME(S) AND ADDRESS(ES)		**10. SPONSORING / MONITORING AGENCY REPORT NUMBER**	

11. SUPPLEMENTARY NOTES

12a. DISTRIBUTION / AVAILABILITY STATEMENT

**Approved for public release;
distribution unlimited.**

13. ABSTRACT *(Maximum 200 Words)*

This research program consisted of two primary research objectives that were aimed at advancing the current understanding of microfluidic processes related to the development of small-scale aircraft and spacecraft.

(1) Develop ultra-high resolution PIV instrumentation for measuring velocity vectors with spatial resolutions approaching one micron and temporal resolutions approaching five nanoseconds for use in measuring microfluidic devices.

(2) Analyze and document the flow physics of several micronozzles with diameters ranging between 50 and 500 μm. The resulting information will be used to motivate, new, more efficient micronozzle designs and validate Navier-Stokes simulations of micronozzles.

The instrumentation being developed in Objective (1) has had a broad impact on the microfluidics community. Specifically, the micro PIV technology can be extended ultimately to analyzing microfluidic devices for non-aerospace applications such as micromixing processes in BioMEMS devices or transient processes in inkjets heads. The results from Objective (2) will provide valuable information for designing many of the key elements required for small-scale aircraft and spacecraft. For example, micronozzles can be used for attitude control and thrust vectoring of small-scale aircraft.

14. SUBJECT TERMS			15. NUMBER OF PAGES
			16. PRICE CODE
17. SECURITY CLASSIFICATION OF REPORT	**18. SECURITY CLASSIFICATION OF THIS PAGE**	**19. SECURITY CLASSIFICATION OF ABSTRACT**	**20. LIMITATION OF ABSTRACT**

Development of micro-resolution PIV and analysis of microthrusters for small-scale aircraft and spacecraft

C. Carl D. Meinhart

Department of Mechanical and Environmental Engineering
University of California

Executive Summary

This research program consisted of two primary research objectives that were aimed at advancing the current understanding of microfluidic processes related to the development of small-scale aircraft and spacecraft.

(1) Develop ultra-high resolution PIV instrumentation for measuring velocity vectors with spatial resolutions approaching one micron and temporal resolutions approaching five nanoseconds for use in measuring microfluidic devices.

(2) Analyze and document the flow physics of several micronozzles with diameters ranging between 50 and 500 μm. The resulting information will be used to motivate, new, more efficient micronozzle designs and validate Navier-Stokes simulations of micronozzles.

The instrumentation being developed in Objective (1) has had a broad impact on the microfluidics community. Specifically, the micro PIV technology can be extended ultimately to analyzing microfluidic devices for non-aerospace applications such as micromixing processes in BioMEMS devices or transient processes in inkjets heads. The results from Objective (2) will provide valuable information for designing many of the key elements required for small-scale aircraft and spacecraft. For example, micronozzles can be used for attitude control and thrust vectoring of small-scale aircraft.

20010404 107

- 1 -

A Particle Image Velocimetry (PIV) system has been developed to measure velocity fields with order one-micron spatial resolution. The technique uses 200 nm diameter flow-tracing particles, a pulsed Nd:YAG laser, an inverted epi-fluorescent microscope, and a cooled interline-transfer CCD camera to record high-resolution particle-image fields. The spatial resolution of the PIV technique is limited primarily by the diffraction-limited resolution of the recording optics. The accuracy of the PIV system was demonstrated by measuring the known flow field in a 30 μm $\times$ 300 μm (nominal dimension) microchannel. The resulting velocity fields have a spatial resolution, defined by the size of the first window of the interrogation spot and by the out of plane resolution of 13.6 μm $\times$ 0.9 μm $\times$ 1.8 μm, in the streamwise, wall-normal, and out of plane directions, respectively. By overlapping the interrogation spots by 50% to satisfy the Nyquist sampling criterion, a velocity-vector spacing of 450 nm in the wall-normal direction is achieved. These measurements are accurate to within 2% full-scale resolution, and are the highest spatially resolved PIV measurements published to date.

In order to obtain these measurements, new PIV interrogation algorithms and theory have been developed. These new algorithms include ensemble-averaged based correlation analysis and central difference interrogation (CDI). The principle of the ensemble correlations is that tremendous gain in signal to noise results from averaging a time-series of particle-image correlation functions, before the signal peak is located. Central difference interrogation allows one to obtain velocity data that is both second order accurate in time and in space. The technique also allows one to obtain velocity data near curved boundaries.

Finally, micro PIV was applied to obtain measurements of liquid flow in silicon micromachined nozzles. The results showed near separation on one of the side walls in the expansion area. Considerable effort was focused on extending the technique from liquid flows in

micronozzles to gaseous flows. This extension to gaseous flows proved to be rather challenging. In particular, it was quite difficult to seed 50 nm glass particles in air flow at the microscale. Furthermore, imaging these small particles proved to be difficult and non-fluorescing imaging techniques, such as DIC were explored.

Supported Personnel

Marin Sigurdson – Associate Laboratory Engineer

Derek Tretheway – Postdoctoral Researcher

Steve Wereley – Postdoctoral Researcher

Mike Gray – Graduate Student Researcher

Hong-Sheng Zhang – Graduate Student Researcher

Yang Lu – Graduate Student Researcher

Publications Resulting from Support

S. T. Wereley and **C. D. Meinhart** 2001. Adaptive second-order accurate particle image velocimetry. Accepted *Experiments in Fluids*

C. D. Meinhart, S. T. Wereley, and M .H. B. Gray 2000. Volume Illumination for two-dimensional particle image velocimetry. *Measurement Science Technology* Volume 11, No 6., pp. 809 - 814.

C. D. Meinhart, S. T. Wereley, and J. G. Santiago 2000. A PIV algorithm for estimating time-averaged velocity fields. *Journal of Fluids Engineering*, Vol. 122, pp. 285 – 289.

C. D. Meinhart, S. T. Wereley, and J. G. Santiago 1999. PIV Measurements of a Microchannel Flow. *Exp. in Fluids*, Vol. 27, pp. 414-419.

C. D. Meinhart, S. T. Wereley, and J. G. Santiago 1999. Micron-Resolution Velocimetry Techniques. In *Developments in Laser Techniques and Applications to Fluid Mechanics*, R. J. Adrian *et al.* (Eds.), Springer-Verlag, Berlin

J. G. Santiago, S. Wereley, **C. D. Meinhart**, D. J. Beebe, & R. J. Adrian 1998. A PIV system for microfluidics. *Exp. Fluids*, Vol. 25 No.4, pp 316-319

Conference Papers Resulting from Support

C. D. Meinhart and S. T. Wereley 2001. Fluid Mechanics Issues at the Microscale, *AIAA Paper 2001-0720*, Reno, NV.

S. T. Wereley, L. Gui and **C. D. Meinhart** 2001. Flow Measurements for the Microfrontier, *AIAA Paper 2001-0243*, Reno, NV.

S. T. Wereley and **C. D. Meinhart** 2000. Accuracy Improvements in Particle Image Velocimetry, Algorithms *Proceedings of the 10th International Symposium on Applications of Laser Techniques to Fluid Mechanics*, Lisbon, Portugal.

S. Stone, **C. D. Meinhart** & S. T. Wereley 2000. A microfluidic-based nanoscope, *Proceedings of μ-TAS 2000*, Enchele, The Netherlands, May 15-18

M. Volpert, **C. D. Meinhart**, I. Mezic, and M. Dahleh 1999. An actively controlled micromixer. *ASME – IMECE'99 MEMS symposium*, Nashville, TN

S. T. Wereley, **C. D. Meinhart**, and M. H. B. Gray 1999. Depth effects in volume illuminated particle image velocimetry. *Proceedings of the Third International Workshop on Particle Image Velocimetry*, Santa Barbara, CA, Sept. 16 – 18

C. D. Meinhart, S. T. Wereley, and J. G. Santiago 1999. A PIV Algorithm for estimating time-averaged velocity fields, *Proceedings of Optical Methods and Image Processing in Fluid Flow, 3rd ASME/JSME Fluids Engineering Conference*, July 18-23, San Francisco, CA

C. D. Meinhart, M. H. B. Gray & S. T. Wereley 1999. PIV measurements of high-speed flows in silicon-micromachined nozzles. *AIAA Paper No. 99-3756*

S. T. Wereley, **C. D. Meinhart**, J. G. Santiago & R. J. Adrian 1998. Velocimetry for MEMS applications. *In the proceedings for the Application of Microfabrication to Fluid Mechanics, ASME International Mechanical Engineering Congress and Exposition*, Anaheim, CA, Nov. 15-20

J. G. Santiago, S. T. Wereley, **C. D. Meinhart**, D. Beebe, and R. J. Adrian 1998. A micron-resolution particle image velocimetry system, *8th International Symposium on Flow Visualization*, Sorrento, Italy

R. J. Adrian, K. T. Christensen, S. M. Soloff, and **C. D. Meinhart** 1998. Decomposition of turbulent fields and visualization of vortices. *Proceedings of the 9th International Symposuim on Applications of Laser Techniques to Fluid Mechanics*, Lisbon, Portugal, July 13-16

C. D. Meinhart, S. T. Wereley, J. G. Santiago, and R. J. Adrian. 1998. Diagnostic techniques for microfluidics research. In *Proceedings of the 9th International Symposium on "Applications of Laser Techniques to Fluid Mechanics"*, Lisbon, Portugal, July 13 – 16

S. T. Werely, J. G. Santiago, R. Chiu, **C. D. Meinhart** & R. J. Adrian 1998 Micro-resolution particle image velocimetry. Micro- and Nano- Fabrication Structures and Devices for Biomedical Environmental Applications, SPIE's BiOS'98- International Biomedical Optics Symposium, Jan. 24-30, San Jose, CA

1. Micro PIV Development

Recently, there has been a growing interest to develop microscale devices that can manipulate and transport relatively small volumes of fluids. These devices have applications in many areas of engineering, including propulsion and power generation of micro-satellites, micro air vehicles, inkjet printer heads, and bioanalytical instruments. The recent surge of microfluidic devices has created a need for diagnostic tools with spatial resolutions on the order of several microns. These diagnostic techniques can be used as engineering tools to measure the flow performance of microfluidic devices, and as general scientific instruments to probe the physics of transport processes at the microscale.

Particle image velocimetry (PIV) is a well-established technique for measuring velocity fields in macroscopic fluid systems (Adrian, 1991). In double-pulsed PIV, positions of flow-tracing particles are recorded at two known times by either illuminating the particles using a pulsed light source, or by illuminating the particles using a continuous light source and gating the light near the camera using a mechanical or electronic shutter. The displacement of the particle images is then estimated statistically by correlating the particle image pairs (Meinhart *et al.*, 1993).

The first successful micro PIV experiment was conducted by Santiago *et al.*, (1998). In that experiment, we used an epi-fluorescent microscope with a continuous Hg-arc lamp, and a Princeton Instruments' intensified CCD camera to record the flow around a nominally 30 μm cylinder in a Hele-Shaw flow cell. A bulk velocity of 50 μm s^{-1} was measured with a spatial resolution of 6.9 μm $\times$ 6.9 μm $\times$ 1.5 μm, based upon the size of the first correlation window and the depth-of-field of the microscope. The flow-tracing particles were chosen to be 300 nm diameter polystyrene particles. These particles were large enough to scatter sufficient light for

recording and to reduce the effects of Brownian motion. The Hg-arc lamp continuously illuminated the particles, and the light signal was gated electronically by the CCD intensifier plate. In this experiment, the CCD array was exposed for $\delta t = 2$ ms, and the time delay between exposures was $\Delta t = 68.5$ ms.

The experimental setup of Santiago et al. (1998) is well suited for situations where high spatial resolution and low-light levels are required, such as investigating flows around living microorganisms. Unfortunately, the minimum exposure time of the CCD camera necessary to record particle images is on the order of several milliseconds, and the time delay between image exposures is on the order of tens of milliseconds. This large time interval between image exposures limits the PIV system to relatively low velocities.

In this paper we describe an alternative approach where a 5 ns pulsed Nd:YAG laser is used to illuminate sub-micron fluorescent particles with ~1 mJ of light energy. The fluorescent images are recorded using a cooled interline transfer $1300 \times 1030 \times 12$ bit CCD camera that is capable of taking back-to-back images within a time interval as short as 500 ns. The CCD camera's pixel spacing is 6.8 μm.

Flow-Tracing Particles

Developing PIV to achieve microscale spatial resolution requires that the particles are chosen small enough to follow the flow faithfully without (1) disrupting the flow field, (2) clogging the microdevice, and (3) producing unnecessarily large images. At the same time, the particles must be chosen large enough so that they scatter sufficient light to be recorded and sufficiently dampen out Brownian motion.

Making accurate PIV measurements with spatial resolutions on the order of several microns requires that the diameter of flow-tracing particles, d_p, be on the order of 100 nm to 300 nm

diameter. If visible light with a wavelength of $\lambda = 532$ nm is used to illuminate the particles, the particle diameter will be smaller than the wavelength of light, i.e. $d_p < \lambda$. In this regime, it is difficult to image particles using normal elastic scattering techniques. However, inelastic scattering techniques, such as epi-fluorescence, can be used to image sub-micron particles. Fluorescently labeled polystyrene particles with diameters of 100 - 300 nm and a specific gravity of $\rho_p = 1.055$ are suitable for many microfluidic liquid-flow applications. The particles can be doped with a fluorescent dye that is tuned to absorb light from a frequency-doubled Nd:YAG laser ($\lambda = 532$ nm), with a peak excitation wavelength of $\lambda_{abs} = 540$ nm and a peak emission wavelength of $\lambda_{emit} = 560$ nm. When sub-micron particles are used to trace slow flows, one must consider errors due to particle diffusion resulting from Brownian motion. A first order estimate of this error relative to the displacement in the x-direction is given by Santiago *et al.* (1998)

$$\varepsilon_B = \frac{\langle s^2 \rangle^{1/2}}{\Delta x} = \frac{1}{u}\sqrt{\frac{2D}{\Delta t}}, \tag{1}$$

where s^2 is the random mean square particle displacement associated with Brownian motion, and D is the Brownian diffusion coefficient, u is the characteristic velocity, and Δt is the time interval between pulses.

Since the errors due to Brownian motion are unbiased, they can be substantially reduced by averaging over several particle images in a single interrogation spot or by ensemble averaging over several realizations. In practice, errors due to Brownian motion place a lower limit on the size of particle that can be used to achieve the desired velocity measurement accuracy. This size is dependent on the characteristic velocity of the experiment.

The required density of flow-tracing particles in micro PIV experiments is commonly on the same order as that for macro PIV experiments. Consider a macro PIV experiment where one uses

a 50 µm diameter particle to seed a water flow, and an interrogation spot size of 1 mm × 1 mm × 1 mm. Assuming an average of 10 particles per interrogation volume are required for adequate measurement signal (using standard autocorrelation techniques), the ratio of particle volume to interrogation spot volume is ~ 0.07%. In the current experiment, there was an average of 2.5 particles per a 13.6 µm × 0.9 µm × 1.8 µm interrogation volume. Given particle diameters of 200 nm, the ratio of particle volume to interrogation spot volume is 0.05%. In order to obtain high quality signal with only 2.5 particles per interrogation spot, we employed a specialized ensemble-averaged correlation technique. The algorithm is used to average over 20 instantaneous correlation functions, before searching for the signal peak. This algorithm increases the number of effective particles per measurement volume, and provides adequate signal for reliable measurements. A complete description of the ensemble-averaged correlation technique is discussed by Meinhart *et al.* (1999).

Imaging and Recording

All optical diagnostic techniques are ultimately limited by the diffraction of light. For micro PIV, the spatial resolution is limited by the effective diameter of particle images when projected back into the flow field. For magnifications much larger than unity, the diameter of the diffraction-limited point spread function, in the image plane, is given by

$$d_s = 2.44 M \frac{\lambda}{2NA}, \qquad (2)$$

where M is the total magnification of the microscope and NA is the numerical aperture of the lens (Born & Wolf, 1997). Using an oil-immersion *Nikon CFI Plan Apochromat* 60x objective lens with a numerical aperture of NA = 1.4, and assuming the wavelength of the recording light is $\lambda \approx 560$ nm, the diameter of the point spread function in our experiment is $d_s \approx 29.3$ μm.

The actual image recorded on the CCD camera is the convolution of the diffraction-limited image with the geometric image (Adrian, 1991). Approximating both the geometric and diffraction-limited images as Gaussian functions, the resulting convolution is a Gaussian function with an effective particle diameter d_e, where

$$d_e = \left[M^2 d_p^2 + d_s^2 \right]^{1/2}.$$ (3)

For a magnification of $M = 60$, a particle diameter of $d_p = 200$ nm, and numerical aperture of $NA = 1.4$, the effective particle image diameter projected onto the CCD camera is $d_e = 31.7$ µm. The effective particle diameter when projected back into the flow is 528 nm. According to Prasad et al. (1993) if a particle image diameter is resolved by 3 - 4 pixels, the location of a particle-image correlation peak can be determined to within $1/10^{th}$ the particle-image diameter. This yields a measurement uncertainty of $\delta x \approx d_e/10M$. For the parameters consider here, the uncertainty reduces to $\delta x \approx 528\,\text{nm}/10 = 52.8\,\text{nm}$.

The fact that one can measure particle displacement to within 53 nm is somewhat surprising. In most microscopic applications, one is primarily interested in determining the shape of small objects. Obviously, the smallest resolvable shape is on the order of the resolution of the microscope. In micro PIV, one knows *a priori* the particle shape and is interested only in determining particle position. By over-sampling the image (i.e. resolving the image with 3-4 pixels across the image diameter), one can determine particle position to within an order of magnitude better resolution than the diffraction-limited resolution of the microscope.

In most PIV applications, the thickness of a laser light sheet, Δz, determines the out-of-plane measurement domain. This thickness is usually chosen to be smaller than the depth-of-field of the recording system, δz. Consequently, all particles illuminated by the light sheet produce in-focus images, reducing background noise in the image field (Adrian, 1991). In micro PIV, one is

often interested in obtaining velocity measurements with out-of-plane resolutions on the order of $1 - 10 \mu m$. Forming a light sheet in a microchannel that is $1 - 10 \mu m$ thick is extremely difficult. Aligning the light sheet so that it overlaps with the in-focus object plane of the image-recording system is nearly impossible. In principle, a light sheet could be formed in a microfluidic device by micromachining optical wave guides and light sheet forming optics directly into the device (Sobek *et al.*, 1994). Because of the added difficulty of integrating micromachined optics into our system, we have chosen an alternative method that uses broad field illumination.

Figure 1 shows schematic of the micro PIV system. The illumination beam is produced by two Nd:YAG lasers manufactured by *New Wave, Inc.* The beam is adjusted by a set of lenses and delivered into an inverted epi-fluorescent microscope, where an optical filter assembly directs the beam to the objective lens. The objective lens relays the light onto the microfluidic device, where it illuminates the entire flow volume. Fluorescent particles in the flow field absorb the green illumination light, $\lambda = 532$ nm, and emit a distribution of red light (approximately $\lambda \sim 560$ nm). The emitted light is imaged through an oil-immersion lens and passed to the fluorescent filter cube, where green light from background reflections is filtered out and the red fluorescence from the sub-micron particles is recorded onto a *Princeton Instruments* cooled interline-transfer CCD camera. The camera is cooled to $T = -15°C$, which lowers the readout noise so the weak fluorescent signal can be measured. The duration of the laser pulse is 5 ns. Within 500 ns after exposure, the image field is transferred to storage pixels on the CCD camera, so that a second image field can be recorded by the CCD camera. After a specified time delay, Δt, a second laser pulse is used to record a second set of particle images onto the CCD camera. Both of these images are then read out of the CCD camera and downloaded to a PC computer for processing.

The depth of field of a microscope system is somewhat arbitrary, because there are several definitions of when an image is considered to be unfocused. Inoué and Spring (1997) estimate the total depth of field as the sum of the depth of field due to diffraction and geometric affects

$$\delta z = \frac{n\lambda}{NA^2} + \frac{ne}{M\,NA},\tag{4}$$

where n is the index of refraction of the immersion medium between the microfluidic device and the objective lens ($n = 1.515$ for an oil immersion lens), λ is the wavelength of light in a vacuum ($\lambda \sim 560$ nm for our fluorescent dye), NA is the numerical aperture of the objective lens, M is the total magnification of the system, and e is the smallest resolvable distance of the image detector (i.e. the pixel spacing for the case of a CCD camera).

The first term in equation (4) is due to diffraction. The length represented by this term is chosen by convention to be one fourth of the total distance between the first intensity minima along the optical axis of the 3-D point spread function (Inoué & Spring, 1997). The NA^{-2} dependence of this term suggests that the depth of field for a high NA imaging system decreases more rapidly than the lateral resolution of the image, as NA increases. For the present experiment, equation (4) yields $\delta z \approx 0.6 \mu m$.

Equation (4) should not be directly applied to determine out of plane resolution for micro PIV systems. A better criterion for out of plane resolution is to determine the distance along the optical axis when a particle becomes sufficiently unfocused so that it only contributes a fraction, say $1/10^{th}$, to the correlation function, compared to a similar particle that is located at the object plane. In our experiment, we estimated the out of plane resolution by focusing the objective lens on a set of particles fixed to a microscope slide, and recording a series of images with the objective lens placed at different axial positions. The out of plane resolution was then estimated by determining the distance the object plane moved to produce sufficiently out of focus particle

images, which could not significantly contribute to particle-image correlation. We estimated our out of plane resolution to be $\Delta z \approx 1.8 \pm 0.5 \mu$m.

The process to determine out of plane resolution should be conducted in a timely fashion to minimize drift in the microscope (Crenshaw, 1998). Since the human eye can accommodate from about 25 cm to infinity, out of plane resolution and depth of field cannot be determined accurately from direct visual observation (Inoué & Spring, 1997).

Lastly, out of focus particle images produce background noise in the image field, which can decrease the signal of the in-focus particles. In order to obtain reliable measurements, the background noise must be minimized by using high dynamic range CCD cameras, applying special image processing algorithms during interrogation, and limiting the number density of particles in the flow field.

Microchannel Measurements

A 30 μm × 300 μm × 25 mm glass rectangular microchannel, fabricated by *Wilmad Industries,* was mounted flush to a 170 μm thick glass coverslip and a microscope slide (see Figure 2). By carefully rotating the glass coverslip and the CCD camera, the channel was oriented to the optical plane of the microscope within 0.2°, in all three angles. The orientation was confirmed optically by focusing the CCD camera on the microchannel walls. The microchannel was horizontally positioned using a high-precision *x-y* stage, and verified optically to within ~ 400 nm using epi-fluorescent imaging and image enhancement.

The glass microchannel was imaged through an inverted epi-fluorescent microscope and a *Nikon Plan Apochromat* oil-immersion objective lens with a magnification $M = 60$ and a numerical aperture NA = 1.4. The object plane was placed at approximately $7.5 \pm 1 \mu$m from the bottom of the 30 μm thick microchannel. The Plan Apochromat lens was chosen for the

experiment, because it is a high quality microscope objective designed with low curvature of field, low distortion, and corrected for spherical and chromatic aberrations (Inoué & Spring, 1997).

Since deionized water was used as the working fluid, the effective numerical aperture of the objective lens was limited to $NA \approx 1.23$. A filtered continuous white light source was used to align the test section with the CCD camera and to test for proper particle concentration. During the experiment, the continuous light source was replaced by the pulsed Nd:YAG laser. A *Harvard Apparatus* syringe pump was used to produce a $200 \mu l \, hr^{-1}$ flow through the microchannel.

The particle-image fields were analyzed using a PIV interrogation program developed specifically for microfluidic applications. The program uses an ensemble-averaging correlation technique to estimate velocity vectors at a single measurement point by (1) cross correlating particle-image fields from twenty instantaneous realizations, (2) ensemble averaging the cross correlation functions, and (3) determining the peak of the ensemble-averaged correlation function. This process is repeated for each velocity vector in the measurement domain. The signal-to-noise ratio is significantly increased by ensemble averaging the correlation function before peak detection, as opposed to either ensemble averaging the velocity vectors after peak detection, or ensemble averaging the particle-image field before correlation. The ensemble-averaging correlation technique is limited to steady or periodic flows. For the current experiment, twenty realizations were chosen because that was more than a sufficient number of realizations to give excellent signal, even with a first interrogation window of only 120×8 pixels.

The signal-to-noise ratio resulting from the ensemble-average correlation technique was high enough that there were no erroneous velocity measurements. Consequently, no vector validation was performed on the data after interrogation. The velocity field was smoothed using a 3×3 Gaussian kernel with a standard deviation of 1 grid spacing in both directions.

Figure 3 shows an ensemble-averaged velocity-vector field of the microchannel. The images were analyzed using a low spatial resolution away from the wall, where the velocity gradient is low, and using a high spatial resolution near the wall, where the wall-normal velocity gradient is largest. The interrogation spots were chosen to be longer in the streamwise direction than in the wall-normal direction. This allowed for a sufficient number of particle images to be captured in an interrogation spot, while providing the maximum possible spatial resolution in the wall-normal direction. The spatial resolution, defined by the size of the first interrogation window was 120×40 pixels in the region far from the wall, and 120×8 pixels near the wall. This corresponds to a spatial resolution of $13.6 \, \mu m \times 4.4 \, \mu m$ and $13.6 \, \mu m \times 0.9 \, \mu m$, respectively. The interrogation spots were overlapped by 50% to satisfy the Nyquist sampling criterion. Consequently, the velocity-vector spacing in the wall-normal direction was 450 nm near the wall. The streamwise velocity profile was estimated by line-averaging the measured velocity data in the streamwise direction. Figure 4 compares the streamwise velocity profile estimated from the PIV measurements (shown as symbols) to the analytical solution for laminar Newtonian flow in a rectangular channel (shown as a solid line). The agreement is within 2% full-scale resolution. The bulk flow rate of the analytical curve was determined by matching the free-stream velocity data away from the wall. The wall position of the analytical curve was determined by extrapolating the velocity profile to zero near the wall.

Since the microchannel flow was fully developed, the wall-normal component of the velocity vectors should be close to zero. The average angle of inclination of the velocity field was found to be small, 0.0046 radians, suggesting that test section was slightly rotated relative to the CCD array. This was corrected mathematically by rotating the coordinate system of the velocity field by 0.0046 radians. The precise location of the wall was more accurately determined by applying the no-slip boundary condition and extrapolating the velocity profile to zero at 16 different streamwise positions (see Figure 3a).

Most PIV experiments have difficulty measuring velocity vectors very close to the wall. In many situations, hydrodynamic interactions between the particles and the wall prevent the particles from traveling close to the wall, or background reflections from the wall overshadow particle images. By using 200 nm diameter particles and epi-fluorescence to remove background reflections, we have been able to make accurate velocity measurements to within about 450 nm of the wall, see Figure 4. The position of the wall can be determined to within 400 nm by direct observation of the image.

2. PIV Algorithm Theory

Ensemble-Average Correlation Analysis

At the microscale, it is difficult to form a light sheet that is only a few microns thick, and even more difficult to align such a light sheet with the objective plane of the recording optics. Therefore, in micro PIV experiments the entire test section volume is illuminated with a cone of light emanating from the recording lens, instead of a commonly used light sheet. This limits the number density of particles that can be used to trace the flow. If the particle density is too high, then background noise from out-of-focus particles will dominate the image and reduce the visibility of in-focus particles. If the particle density is too low, then standard cross correlation techniques will fail to provide an adequate signal, causing the measurements to be noisy and sometimes unreliable.

Since many of the low Reynolds number flows in microfluidic devices are laminar and either steady or periodic, it is not necessary to determine instantaneous velocity information. For many of these flows, it is sufficient to measure only the time-averaged or phase-averaged velocity field. In principle, these flow fields can be measured using high-resolution pointwise techniques such as the dual beam laser Doppler anemometer (LDA) system developed by Tieu, Machenzie & Li (1995). This LDA system uses low *f-number* optics to focus the probe volume down to approximately 5 μm $\times$ 10 μm. The micron-resolution LDA technique has advantages over the micro-PIV technique in that one does not have to deal with out of focus particle images, and that one can obtain large numbers of velocity measurements in real time. Micro PIV has advantages over micro LDA in that it does not require alignment of laser beams inside a microfluidic device, and it does require sweeping the probe volume throughout the measurement domain. In

addition, micro PIV takes advantage of the high signal to noise offered by fluorescence imaging.

We present a PIV algorithm that directly estimates time-averaged or phase-averaged velocity fields. The algorithm can provide reliable measurements in low signal-to-noise conditions, where standard cross correlation techniques fail. The PIV algorithm is demonstrated by measuring flow in a 30 μm × 300 μm microchannel flow.

Decomposition of the Correlation Function

The auto correlation function of a single-frame double-exposure particle image field, $I(X)$, is defined as

$$R(s) = \iint I(X)\, I(X+s)\, \mathrm{d}^2 X \quad , \tag{5}$$

where X is the spatial coordinate in the image plane and s is the spatial coordinate in the correlation plane.

$R(s)$ can be decomposed into the following components

$$R(s) = R_c(s) + R_P(s) + R_F(s) + R_{D^-}(s) + R_{D^+}(s), \tag{6}$$

where R_c is the convolution of mean image intensity, R_P is the pedestal component resulting from each particle image correlating with itself, and R_F is the fluctuating component resulting from the correlation between fluctuating image intensity with mean image intensity (Adrian, 1988). The positive and negative displacement components are R_{D^+} and R_{D^-}, respectively.

The signal used to measure displacement is contained only in the R_{D^+} component. Consequently, contributions from all other components of the correlation function may bias the measurements, add random noise to the measurements, or even cause erroneous

measurements. Therefore, it is desirable to reduce or eliminate all the other components. If both exposures of a double-pulse particle image field are recorded separately as a double-frame image field, then the particle images can be interrogated using cross correlation (Keane & Adrian, 1992). In the case of double-frame cross correlation, the R_P and R_{D^-} components do not exist. Further improvements in signal quality can be obtained by image processing. By subtracting the mean image intensity at each interrogation spot before correlation, the R_C and $R_F(s)$ components are set identically to zero, leaving only the positive displacement component, R_{D^+}, in the correlation function.

While the R_{D^+} component is commonly considered the signal component, it contains both noise and signal information. In order to make accurate measurements, the signal-to-noise ratio in the R_{D^+} component must be sufficiently high. This paper presents a method in which the signal-to-noise ratio can be maximized when one is interested in measuring average displacement fields.

Methods of Estimating Average Velocity Fields

Average velocity fields can be obtained by first measuring instantaneous velocities and then averaging them in either space or time. Here we present an alternative method for measuring average velocity fields directly from the correlation function.

Estimation of velocity-vector fields using PIV involves three primary steps:

1. Particle Image Acquisition

2. Particle Image Correlation

3. Correlation Peak Detection

In order to obtain an average velocity measurement, one must apply an averaging operation. The averaging operator is a linear operator, and can be applied after step (1), step (2), or step (3), to produce a non-biased estimate of average velocity. The particle-image correlation and peak detection operations are both nonlinear, and the order in which the averaging operator is applied can dramatically change the quality of the resulting signal.

In this section we examine the three different methods for calculating average velocities based upon the order in which the averaging operator is applied. Here we assume that two single exposure images, *Image A* and *Image B*, are separated by a known time delay, Δt, and represent the image acquisition of a single realization. Furthermore, a sequence of two images is acquired at N different realizations of a statistically stationary process. We wish to average over the N realizations to estimate the average velocity.

Average Velocity Method

In this method, the estimate of the average velocity is determined by, (1) correlating *Image A* and *Image B*, (2) detecting the peak from the instantaneous correlation functions, and (3) averaging over the instantaneous velocity measurements. Figure 5a graphically depicts this process. The primary advantage of this method is that one can obtain instantaneous velocity measurements, which may be of physical importance. However, if one is primarily interested in the average velocity field, this method may not be optimal.

The nonlinear operation of peak detection is susceptible to producing erroneous measurements when the signal to noise is low in the instantaneous correlation. In practice, the vector fields must be validated by identifying and removing erroneous

velocity measurements (Meinhart *et al.*, 1994; Westerweel, 1993). Without vector validation, all the instantaneous measurements must be reliable in order to obtain a reliable average velocity measurement. For situations where the particle image density is low, there may not be adequate signal to obtain valid measurements from the instantaneous correlation functions. In these situations, the alternative methods described below may be employed.

Average Image Method

In this method, the averaging operation can be performed directly on image fields A and B, and then correlated to obtain $R_{\overline{AB}}$. This process is depicted graphically in Figure 5b. In the situation where particle image number density is low, averaging the image fields together can increase the average number of particles per interrogation spot. However, excessive averaging of the image fields can create too many particle images in the interrogation spot and reduce the visibility of individual particle images.

The 2-D spatial correlation function of the average of A and B image fields is defined as

$$R_{\overline{AB}}(s) = \iint \overline{A}(X)\overline{B}(X+s)\, d^2X, \tag{7}$$

where $\overline{A} = \dfrac{1}{N}\displaystyle\sum_{i=1}^{N} A_i$ is the average operator, averaging over N realizations of the flow field. Expanding the integrand of (7) yields

$$R_{\overline{AB}}(s) = \iint \begin{bmatrix} A_1B_1 + A_1B_2 + A_1B_3 + \bullet\bullet\bullet + A_1B_N + \\[4pt] A_2B_1 + A_2B_2 + A_2B_3 + \bullet\bullet\bullet + A_2B_N + \\[4pt] A_3B_1 + A_3B_2 + A_3B_3 + \bullet\bullet\bullet + A_3B_N + \\ \bullet \qquad\qquad \bullet \qquad \bullet \\ \bullet \qquad\qquad\quad \bullet \qquad \bullet \\ \bullet \qquad\qquad\qquad \bullet \quad \bullet \\ A_NB_1 + A_NB_2 + A_NB_3 + \bullet\bullet\bullet + A_NB_N \end{bmatrix} d^2X \,. \tag{8}$$

Following the discussion of previous section, if A and B represent paired single-exposure image fields separated by a known time interval, Δt, which are cross correlated, and if the mean image intensity is subtracted before correlation, then all $N \times N$ terms in (8) are contained in the R_D component of R.

Only the N diagonal terms in (8) contribute to signal. The $N(N-1)$ off diagonal terms represent random particle correlation across different realizations, which produce noise in the correlation function that can reduce the accuracy of the measurement and cause erroneous measurements. Since the off diagonal terms are random and uniformly distributed throughout the correlation plane, they may or may not contaminate the signal peak. The number of noise terms increases as N^2, while the number of signal terms increases as N.

In demanding situations when particle-number density is low, or when small interrogation regions are chosen to produce high spatial resolution, it may be impossible to obtain an adequate signal from instantaneous cross correlation analysis. Clearly, averaging the particle-image fields over several realizations and then correlating can increase the signal-to-noise ratio. However, if the number of realizations used in the average is beyond an optimal number, the signal-to-noise ratio can be reduced by further increases in N. Loss of signal occurs because the number of non-diagonal (noise) terms

increases faster than the diagonal (signal) terms. The optimal number of realizations depends upon many factors including interrogation spot size, particle-image number density, and particle-image quality.

Average Correlation Method

A third method for estimating average displacement fields is to calculate instantaneous correlation functions, average the correlation function, and then determine the location of the signal peak location. The *Average Correlation Method* is shown graphically in Figure 5c. The average of instantaneous correlation functions over N realizations can be written as

$$\overline{R}_{AB}(s) = \overline{\iint A(X)B(X+s)\mathrm{d}^2 X} \\ = \iint \overline{A(X)B(X+s)}\mathrm{d}^2 X . \tag{9}$$

Figure 6 shows several instantaneous correlation functions, and an average correlation function calculated by averaging 20 instantaneous correlation functions. The instantaneous correlation functions are characteristic of micro PIV data and were obtained from an actual micro PIV experiment. The instantaneous correlation functions contain significant amounts of noise that can lead to inaccurate or unreliable measurements. This noise is substantially less in the average correlation function.

Since the operations of averaging and the integration commute, the average operator can be taken inside of the integral so that

$$\overline{R}_{AB}(s) = \iint \left[A_1 B_1 + A_2 B_2 + A_3 B_3 + \bullet\bullet\bullet + A_N B_N \right] \mathrm{d}^2 X . \tag{10}$$

From (10), the average correlation function contains only the diagonal (i.e. signal) terms of (8). Therefore, this type of average produces a much higher signal-to-noise ratio

than the alternative methods that have been discussed previously. The number of signal terms increase linearly with the number of realizations, N. Unlike the average image method, there is no penalty for including large numbers of realizations in the average. Since the average operator is applied to the correlation function before peak detection, the probability of erroneous measurements is greatly reduced.

Application to Microchannel Flow

The three different averaging algorithms were applied to a series of particle image fields taken of steady Stokes' water flow through a 30 μm × 300 μm glass microchannel. Details of the same experiment but for a different flow rate are discussed by Meinhart *et al.* (in press). The out of plane measurement resolution is related to the depth of field of the microscope optics, and is estimated to be approximately 1.8 μm. Based on the discussion of Santiago *et al.* (1998), the error due to Brownian motion for a single particle is estimated to be less than 3% full-scale error. The interrogation spot size was 16 × 64 pixels and 24 × 72 pixels, for window 1 and window 2, respectively. The relative offset between the windows was adjusted adaptively to approximate the particle image displacement at each measurement location. The interrogation windows were chosen to be small and have a high aspect ratio to achieve high spatial resolution in the wall-normal direction.

The signal-to-noise ratio from standard correlation techniques was relatively low, because there was an average of only 2.5 particle images located in each 16 × 64 pixel interrogation window. The signal-to-noise ratio could be improved by increasing the size of the correlation windows, but with reduced spatial resolution. Alternatively, the particle

concentration in the flow field could be increased, but that would increase the number of out of focus particles, and produce more background image noise.

Figure 7a shows an instantaneous velocity-vector field, calculated using a standard cross correlation technique without any type of vector validation or smoothing applied to the field. The velocity measurements contained in the row closest to the wall are not considered to be accurate, because part of their interrogation region lies outside the flow domain. The velocity measurements are noisy, and approximately 20% appear to be erroneous. An average over 20 instantaneous velocity fields is shown in Figure 7b. Averaging reduces small random noise in the instantaneous fields. However, the large errors associated with the erroneous measurements are not averaged out quickly. The application of vector validation algorithms can usually eliminate errors due to erroneous measurements producing accurate velocity measurements, however *a priori* knowledge of the flow field is required.

The same series of double-frame particle image fields were correlated, the correlation functions were averaged, and then the locations of the signal peaks in the correlation plane were determined, following the *average correlation method* depicted in Figure 5c. The resulting velocity-vector field is shown in Figure 7c. No vector validation or smoothing has been applied to this field. The field contains only $0.5 - 1$ % erroneous measurements and has less noise than the vector fields shown in Figures 7a and 7b.

The relative performance of the three averaging algorithms was quantitatively compared by varying the number of realizations used in the average, from one to twenty. The fraction of valid measurements for each average was determined by identifying the number of velocity measurements in which the streamwise component of velocity

deviated by more than 10% from the known solution at each point. For this comparison, the known solution was the velocity vector field estimated by applying the average correlation technique to 20 realizations, and then smoothing the flow field.

Figure 8 shows the fraction of valid measurements for each of the three algorithms as a function of the number of realizations used in the average. The average correlation method outperforms the other two methods, and produces less than $0.5 - 1\%$ erroneous measurements after averaging eight realizations. The average image method produces about 95% reliable velocity measurements, and reaches a maximum at four averages. Further increases in the number of realizations used to average the images decreases the signal to noise of the average particle-image field, and produces noise in the correlation plane due to random correlation between non-paired particle images. The average velocity method reaches a maximum of 88% reliable measurements using two velocity averages. Further increases in the number of averages decreases the number of reliable measurements, due to an increase in the probability of an encountering an erroneous measurement.

Central Difference Interrogation

Since the early days of particle image velocimetry (PIV), researchers have realized that PIV algorithms do not generally make maximal use of the information contained in the images they interrogate. In particular, Spedding and Rignot (1993) observed that the most appropriate spatial location for the displacement vector calculated by measurement techniques which track the motion of tracer particles, such as PIV, is displaced from the centroid of the first interrogation region by a distance equal to half the displacement vector, and not at the centroid of the first interrogation region (as is commonly implemented). Attributing the displacement measurement to its proper location is equivalent to a central difference approximation (order Δt^2) to the velocity field whereas the conventional implementation of PIV is equivalent to a forward difference approximation (order Δt). Wereley, *et al*, (1998) and Lourenco and Krothapalli, (1998) both implemented second order accurate PIV techniques without proof of their effectiveness. Unfortunately, moving the measured displacement vector from the centroid of the first interrogation region destroys the uniform spacing of the measured displacement data that most researchers prefer. Because other velocimetric techniques, such as particle tracking velocimetry and scalar image velocimetry, also produce non-uniformly spaced data, several researchers in fields related to PIV have addressed how to map non-uniformly spaced data onto a uniform grid and what are the effects of doing so (Spedding and Rignot, 1993, Agui and Jimenez, 1987, Cohn and Koochesfahani, 1999). Regardless of the accuracy, the remapping process will always introduce some error into the measurement.

In this paper we will explore another approach, namely adaptively shifting the locations of the first and second interrogation regions such that when the calculated displacement vectors are located at their most proper locations (displaced from the

centroids of the first interrogation regions by half the displacement distance), they will occur on a uniformly spaced grid, preserving the accuracy of the original calculations and eliminating the need for remapping. We will present an adaptive, iterative, second order accurate PIV algorithm which significantly improves spatial resolution and overall accuracy while reducing velocity bias errors in comparison to conventional PIV algorithms. This algorithm was initially developed by Wereley, *et al.* (1998) and presented without demonstrating its second order accuracy. Here the analysis is expanded and a theoretical, computational and experimental analysis of the algorithm will be given. We will consider two component PIV in which the images are recorded as pairs of singly-pulsed images on consecutive frames of some digital medium (CCD camera typically). Most of the ideas considered here are extensible to other forms of two component and three component PIV.

Spatial Resolution

The spatial resolution of any physical measuring system can be generally defined as the volume of space required to make the measurement. Similarly, the temporal resolution of a measurement system can be defined as the total amount of time over which the measurement is averaged. Using these definitions, the spatial resolution of cross-correlation PIV is determined by the size of the interrogation windows used to interrogate the images and the spatial shift between the interrogation windows. The temporal resolution is the time between each image exposure. Generally, the spatial resolution κ is a three-dimensional function of position that can be expressed as

$$\{\kappa_x, \kappa_y, \kappa_z\} = \{\min(W_{x1}, W_{x2}) + |\Delta X|, \min(W_{y1}, W_{y2}) + |\Delta Y|, \delta z_c\} \tag{11}$$

where W_{x1} and W_{y1} represent the size of the first interrogation window and W_{x2} and W_{y2} represent the size of the second interrogation window. The spatial shift between first and second interrogation windows in the x direction is represented by ΔX and in the y direction by ΔY. The quantity δz_c represents the depth of the measurement domain in the out of plane direction. These parameters can be constants and express the overall spatial resolution for the entire image or they can vary from measurement point to measurement point and produce a spatial resolution which varies across the region of interest.

The typical constraint that the difference between the particle displacement and the spatial offset between first and second interrogation regions not exceed 1/3 of the interrogation region size can be eliminated by always using a spatial shift equal to the local flow velocity. The window size W can be chosen by signal strength or spatial gradient considerations alone. Keane and Adrian (1993) were the first to suggest such an approach and performed the theoretical calculations to show that this method would be superior to other methods. Urushihara, Meinhart, and Adrian (1993) first implemented a simple, flexible spatial shifting technique. The second order accurate adaptive technique presented here is similar in nature to the first order accurate technique of Cowen and Monismith (1997), who implement a multi-pass adaptive spatial shift as part of their super resolution particle tracking routine. At every measurement point they started with an initial estimate of the velocity at that point which was used as the spatial shift. The resulting velocity measurement was then used in the next iteration as the spatial shift. Measurement points at which this procedure did not converge to a constant spatial shift within three iterations were flagged as invalid.

Accuracy

The issue of accuracy is related to that of spatial resolution. Larger interrogation windows and larger spatial shifts will clearly produce more coarse estimations of the local or instantaneous velocity field. However, simply minimizing the size of the interrogation windows or the distance the particles move between the two images is not the solution because a certain minimum number of particle images are required to produce reliable measurements in any given experimental situation. In addition, those particles must move a sufficient distance to reduce the relative error in determining the location of the correlation peak to acceptable levels. One solution is to use a higher-order approximation velocity calculation. To take advantage of the existing specialized equipment for acquiring image pairs—double pulse lasers and interline transfer cameras—it is necessary to limit the data acquisition to pairs of images. Most PIV algorithms use a simple forward differencing interrogation (FDI) scheme in which the velocity at time t is calculated using particle images recorded at times t and t+ Δt, given by

$$V(t) = \frac{d\mathbf{X}}{d\tau}\bigg|_{\tau=t} = \frac{\mathbf{X}(t+\Delta t) - \mathbf{X}(t)}{\Delta t} + \frac{\Delta t}{2}\frac{d^2\mathbf{X}}{d\tau^2}\bigg|_{\tau=t} + \ldots \tag{12}$$

The accuracy of the velocity calculation can be greatly improved by using a relatively simple central differencing interrogation (CDI) scheme in which the velocity at time t is calculated using particle images at times t-Δt/2 and t+ Δt /2, given by

$$V(t) = \frac{d\mathbf{X}}{d\tau}\bigg|_{\tau=t} = \frac{\mathbf{X}(t+\Delta t/2) - \mathbf{X}(t-\Delta t/2)}{\Delta t} + \frac{(\Delta t)^2}{24}\frac{d^3\mathbf{X}}{d\tau^3}\bigg|_{\tau=t} + \ldots \tag{13}$$

The velocity approximation is accurate to order Δt for the forward difference formulation while the central difference formulation is accurate to order Δt² using the same two images. This

improved accuracy can correspond to better accuracy for a given time delay or allow increasing the time delay between images while maintaining a desired accuracy. The relative contribution of other errors, such as Brownian motion or the uncertainty in finding the correlation peak location, to the overall error can then be reduced.

Velocity Bias

One area where measurement errors can be significantly reduced at little additional computational expense is velocity bias. PIV measurements made with equally-sized interrogation windows in the first and second images are generally biased towards the spatial shift of the interrogation windows. Westerweel (1997) demonstrates that this error is on the order of 0.1 pixels for common PIV parameters—32×32 pixel interrogation windows, particle diameters in the range of 2 to 4 pixels, 10 particle images per interrogation window, and displacements ranging from 0 to 10 pixels. Westerweel also demonstrates that this error decays linearly to zero as the particle displacement decreases from 0.5 pixels to zero pixels. While this error may seem relatively insignificant, it can seriously degrade the calculation of derivative quantities such as vorticity and shear stress. Even though the velocity bias error becomes very small for displacements smaller than 0.5 pixels, Huang, *et al.* (1997) demonstrate that simply spatial shifting identically-sized interrogation windows is insufficient to fully eliminate velocity bias. The velocity bias can be eliminated by several techniques. Westerweel (1993) demonstrates that dividing the image correlation function by the correlation of the windowing functions, commonly denoted F_I, will completely eliminate the velocity bias. Recently, Huang, *et al.* (1997) demonstrated an efficient algorithm that eliminates velocity bias errors by renormalizing the values of the correlation function in the vicinity of the peak location prior to calculating the subpixel peak location.

Keane and Adrian (1993) suggest that bias errors can be nearly eliminated by making the second interrogation window sufficiently larger than the first so that all particle images in all first interrogation windows will likely be contained in the second. They also propose that spatially-shifting the second interrogation window by the integer part of the displacement will substantially reduce this error. In a further analysis of Keane and Adrian's theory, Westerweel (1997) points out that using interrogation windows of differing sizes results in a constant-valued portion at the center of the window correlation function F_I, corresponding to small displacements, which eliminates the velocity bias. Since our adaptive procedure uses spatial shifts that very accurately reflect the velocity of the particles in the interrogation windows, the approach suggested by Keane and Adrian can be implemented with minimal computational expense by making one of the interrogation windows as little as 2 pixels larger than the other in each direction. Because the application of our technique is measuring microscale flows in which Brownian motion of the seed particles can be a serious factor, we typically make the second interrogation window larger than the first to account for possible diffusion of the tracer particles. The size of the second interrogation window is increased by the number of pixels that particle diffusion and spatial gradients are expected to affect the flow plus a few additional pixels, typically two, in each direction to produce the constant-valued region at the center of the window correlation function.

Ensemble-Averaged Correlation Function

For both the experimental and simulated flows presented here, an ensemble of image pairs is acquired or generated which can be interrogated at higher spatial resolution than single pairs of images. Consequently the effect of the spatial averaging inherent in PIV measurements is reduced, allowing the accuracy of the central differencing algorithm to be fully explored. The

standard method for determining ensemble-averaged flow fields is to obtain a series of instantaneous velocity fields and then ensemble average them. When the signal-to-noise ratio of the images is low, which can happen for a variety of reasons, such as faint seed particle images, high background noise, and Brownian motion of seed particles, this procedure can produce many spurious vectors, called 'outliers', due to the peak search algorithm mistakenly identifying a noise peak as the signal peak. These outliers can be located anywhere in the correlation plane and are completely uncorrelated with the signal peak location. Consequently they can cause significant noise. Often these vectors can be eliminated from the ensemble by using statistical arguments. Even so, it is preferable for these outliers not to be created in the first place.

Recently, Meinhart, Wereley, and Santiago (2000) demonstrated a novel ensemble averaging technique for improving the signal-to-noise ratio of steady-state velocity measurements. Instead of ensemble averaging after the calculation of the series of velocity fields, at every measurement point they ensemble averaged the correlation function before the peak search algorithm was performed. By ensemble averaging in this way, the signal peaks add constructively while the randomly distributed noise peaks do not, making the signal peak more distinguishable from the noise peaks. This procedure computes an ensemble averaged velocity field without first calculating the instantaneous velocity field. One of the primary advantages of ensemble averaging in this manner is that the effective particle image concentration is increased, which allows for reducing the size of the interrogation windows. In the experiments and simulations described in Section 4, 26 image pairs were acquired or generated which allowed the spatial resolution to be increased to the point at which 20 statistically-independent measurements can be made across the relatively narrow gap of a cylindrical Couette flow system.

Central Difference Interrogation Fundamentals

A central difference interrogation (CDI) scheme has many advantages over the conventional forward difference interrogation (FDI) scheme. The most obvious advantage already mentioned is that the technique is second order accurate, providing increased accuracy over the forward difference scheme for the same time delay or, alternately, the same accuracy as the forward difference scheme for a significantly longer time delay. In many situations it is advantageous to use a larger time delay. For example, in microscale flows the diffusion of submicron seed particles may be a significant source of error for microscale velocity measurements (Santiago, *et al.*, 1998). The error associated with Brownian motion ε_B was shown to be

$$\varepsilon_B = \frac{1}{u}\sqrt{\frac{2D}{\Delta t}} \tag{14}$$

where u is the local velocity, D is the diffusion coefficient of the particles, and Δt is the time delay. Equation 14 demonstrates that when all other factors remain constant the relative error due to Brownian motion can be reduced by increasing the time delay.

Further advantages of the CDI algorithm are that it allows velocity field to be calculated closer to flow boundaries as well as in a symmetric manner with respect to flow boundaries. These advantages can be demonstrated by examining the following stagnation type flow. Figures 9a and 9b show velocity fields of a flow around a human red blood cell calculated by an adaptive spatial shift FDI scheme and also by the adaptive spatial shift CDI scheme. These results were taken from a set of experiments conducted by Juan Santiago at the Beckman Institute at the University of and are described further by Wereley, et al. (1998). The blood cell is trapped between a coverslip and a slide glass and surrounded by deionized, particle seeded water (300 nm diameter polystyrene latex, 10^{-4} concentration by volume). The flow is driven from lower

left to upper right around the blood cell using the surface tension of a water droplet placed at the edge of the coverslip to establish a flow past the blood cell. The images are interrogated with 28×28 pixel interrogation windows that are overlapped by 75%. While this overlap oversamples the images, it functions as a very accurate (yet computationally inefficient) interpolator of the velocity field. For both algorithms, measurement regions that resulted in more than 20% of the combined area of the first and second interrogation windows inside of the blood cell are eliminated and replaced with an 'x' symbol because they will tend to produce velocity measurements with serious errors. The CDI scheme is able to accurately measure velocities closer to the surface of the cell than is the FDI scheme. The CDI scheme has a total of 55 invalid measurement points, equivalent to 59.4 μm^2 of image area that cannot be interrogated, while the forward difference has 57 invalid measurement points or 61.6 μm^2. Although this difference of two measurement points may not seem significant, it amounts to the area that the FDI algorithm cannot interrogate being 3.7% larger than the area the CDI algorithm cannot interrogate. Furthermore, the distribution of the invalid points is significant. By carefully comparing Figure 9a with 9b, it is apparent that the FDI has three more invalid measurement points upstream of the blood cell than does the CDI scheme while the CDI scheme has one more invalid point downstream of the blood cell. This difference in distribution of invalid points translates into the centroid of the invalid area being nearly twice as far from the center of the blood cell in the FDI case (0.66 μm or 7.85% of the cell diameter) versus the CDI case (0.34 μm or 4.05% of the cell diameter). This difference means that the FDI measurements are less symmetrically distributed around the blood cell than the CDI measurements are. In fact, they are biased toward the time the first image was recorded. Computing the average distance between the invalid measurement points and the surface of the blood cell indicates how closely to the blood cell surface each

algorithm will allow the images to be accurately interrogated. On average the invalid measurement points bordering the red blood cell generated using the FDI scheme are 12% farther from the cell than the invalid measurement points generated with the CDI scheme. Consequently, the adaptive CDI algorithm is more symmetric than the adaptive FDI algorithm and also allows measuring the velocity field nearer the cell surface.

Central Difference Interrogation Algorithm

The forward difference scheme (conventional PIV) can be easily implemented using a constant spatial shift in a single iteration, while the central difference scheme requires a more complicated algorithm. In general, the goal of PIV is to measure a velocity field that contains spatial gradients. These spatial gradients translate into particles moving at different velocities as a function of spatial position. In order to define the measurement time t as halfway between $t-\Delta t/2$ and $t+\Delta t/2$, the spatial shift between interrogation windows at each measurement point in the first and second image must be equal to the distance the particles move between images, just as in conventional forward difference algorithms. In practice, a uniformly-spaced grid of measurement points is defined at the time t and the interrogation windows in the first image are shifted by an amount $-\bar{V}(x,y)\cdot\Delta t/2$ while the interrogation windows in the second image are shifted by an amount $+\bar{V}(x,y)\cdot\Delta t/2$, netting a spatial shift of $\bar{V}(x,y)\cdot\Delta t$ centered between the particle locations in the first and second images. Clearly, employing this variable spatial shift requires an advanced knowledge of the velocity field. An iterative adaptive approach is required in which increasingly accurate estimates of the velocity field are used to compute the spatial shift, in turn yielding increasingly accurate velocity field estimates.

This procedure is outlined in flowchart form in Figure 10. The first step in the procedure is to obtain a low spatial resolution measurement of the entire velocity field using a constant spatial shift between all first and second interrogation windows at every measurement point. This coarse measurement provides an initial estimate of the velocity field. In the case of the Couette flow measurements, 64 pixel square interrogation windows with a spatial shift between first and second interrogation windows equal to the estimated mean displacement of the particles in the images was used. No overlap between neighboring windows was used. After the velocity field was calculated, the vectors were validated using CleanVec[1]. CleanVec compares a candidate measurement with the median of its neighbors' values to determine whether it is more likely a valid measurement or an invalid measurement attributable to noise. If a vector differs from the median of its neighbors by more than an amount specified by the user, it will be replaced by either the second choice or third choice correlation peak which are found along with the primary correlation peak and stored for error correction purposes. If neither of these secondary peaks matches the neighborhood any better, a vector is calculated by interpolating from the neighbors' values. Gaussian smoothing is used to remove noise in the displacement field.

Using the initial validated velocity field measurement, a grid of new measurement points is chosen for subsequent high spatial resolution interrogation of the images. A bicubic interpolation scheme is used to resample the initial low resolution velocity field at each new high resolution measurement point. This step is used purely as an initial estimate of the high resolution velocity field and is the only interpolation step in the algorithm. When using a forward difference formula to approximate the velocity, each measurement point is located at the centroid of each first interrogation window. In the central difference formulation, however, the

measurement point is located halfway between the centroids of the first and second interrogation windows. At each measurement point in the CDI algorithm, the centroid of the first interrogation window is displaced from the location of the measurement point by the integer number of pixels that is nearest $-0.5*\Delta X$, i.e. opposite to the flow direction, while the centroid of the second interrogation window is displaced from the first by the integer number of pixels nearest ΔX. Here ΔX represents the local expected displacement measurement from a previous iteration. The grid of measurement points is chosen so that the maximum area of the images is interrogated without any of the interrogation windows going beyond the edges of the images. The new high resolution displacement field is then calculated using the interpolated displacement field to determine the spatial shifting of the interrogation windows. After each iteration, the vectors are checked for convergence to see if the velocity field is progressing to a value that does not change between iterations. If another iteration is needed, the data are validated again. If not, the data are usually of high enough quality that further post-processing is not necessary.

Application to Cylindrical Couette Flow

In order to study the relative accuracy of different PIV algorithms, it is necessary to compare the results from interrogating a known velocity field using each of the different schemes. The scheme producing results that most closely match the known velocity field will be the more accurate one. Two adaptive image shifting techniques will be compared. The first is a conventional forward difference interrogation (FDI) scheme and the second is the new central difference interrogation (CDI) scheme. These two adaptive techniques both require only two images to compute and approximately the same amount of computational effort when compared to each other but do require additional computational effort when compared with constant shift

techniques. Cylindrical Couette flow is used as a test bed to compare the two PIV algorithms because it is a relatively simple flow with a closed-form solution in which experimental velocity measurements can be compared to Monte Carlo simulated images and analytical calculations to determine the relative accuracy of each technique.

Cylindrical Couette flow is produced between two differentially rotating concentric cylinders. The steady state velocity field is nearly one-dimensional far from the ends of the apparatus and obeys the simple and well known solution to the Navier-Stokes equations

$$
\begin{aligned}
v_r &= v_z = 0 \\
v_\theta(r) &= r \cdot \omega(r) = A_0 \cdot r + B_0/r
\end{aligned}
\tag{15}
$$

where v_r, v_θ, and v_z are the radial, azimuthal, and axial velocity components, respectively, r is the radial position, ω is the angular velocity, and the no-slip boundary conditions at the inner and outer cylinder uniquely determine the constants A_0 and B_0. Since the velocity field is known, a flow can be simulated by evolving randomly-distributed particles forward in time using the velocity field in Equation (15). Wereley and Lueptow (1994, 1998), among others, have shown that experimental measurements of this flow very closely approach the analytical solution, making it a good candidate for comparing simulated flows to experimental results.

Forward Difference Error Evaluation

Because PIV is usually performed on a Cartesian grid while cylindrical Couette flow exhibits azimuthal symmetry, notation can become somewhat confusing. To bridge this notational gap, we will consider a fluid element located at the Cartesian coordinates (X_0, Y_0) which coincide with the polar coordinates (r_0, θ_0) (see Figure 11a). The angular velocity of the fluid element at a position r_0 is given by $\omega(r_0)$. This fluid element will be swept through an arc of length $r_0\omega(r_0)\Delta t$

during the time Δt to the new position (X_1, Y_1) which coincides with (r_0, θ_1). Because the velocity field is independent of azimuthal position, we can, without loss of generality, set $\theta_0 = 0$ for the remainder of the analysis to simplify the mathematics. The standard first order accurate forward difference discretization of the velocity field is

$$\bar{V}_{meas} = \frac{\bar{X}(t + \Delta t) - \bar{X}(t)}{\Delta t} \tag{16}$$

Since the fluid elements trace out curved paths, and this discretization is a two point, linear approximation to the derivative, there will necessarily be some discrepancy between the measurement and the actual velocity. In order to compare the two PIV algorithms, we will quantify this error for both schemes. The Cartesian components of the velocity field can be written as

$$V_{x,meas} = \frac{X_1 - X_0}{\Delta t} = \frac{r_0 \cos\{\omega(r_0)\Delta t\} - r_0}{\Delta t} \tag{17a}$$

$$V_{y,meas} = \frac{Y_1 - Y_0}{\Delta t} = \frac{r_0 \sin\{\omega(r_0)\Delta t\}}{\Delta t} \tag{17b}$$

The actual instantaneous velocity at the point (X_0, Y_0) can be written as

$$\begin{aligned} V_{x,act} &= 0 \\ V_{y,act} &= r_0 \omega(r_0) \end{aligned} \tag{18}$$

The difference between these two velocities will tell us how much of an effect the limitations of the PIV algorithm will have on the overall accuracy of the measurements. To simplify the resulting expression, the trigonometric functions will be expanded as power series. After significant algebraic manipulation, the error in the X and Y direction are found to be

$$\Delta V_x = -\frac{1}{2} r_0 \Delta t \cdot \omega(r_0)^2 + \frac{1}{24} r_0 \Delta t^3 \omega(r_0)^4 + \dots$$

$$\Delta V_y = -\frac{1}{6} r_0 \Delta t^2 \omega(r_0)^3 + \frac{1}{120} r_0 \Delta t^4 \omega(r_0)^5 + \dots \qquad (19)$$

where ΔV_x and ΔV_y represent the bias error in each direction.

The error in X (or radial) component is proportional to Δt while the error in the Y (or azimuthal) component is proportional to Δt^2. In a general flow with no particular symmetry, the error in both components should be order Δt, but the azimuthal symmetry in this flow increases the accuracy of the azimuthal component to order Δt^2. In the special case of measuring Couette flow, it is not necessary to measure the radial velocity component since it should be zero (unless to verify that the experiment is properly aligned). However, in cases where higher-order flow states are being measured, such as Taylor vortex flow and wavy Taylor vortex flow, where the radial velocity component is of interest and is much smaller than the azimuthal component, first order accuracy in Δt can be restrictive.

Central Difference Error Evaluation

Although the CDI technique is ostensibly second-order accurate in Δt, the accuracy of the technique must be carefully examined to prove its advantages. Toward this end, we will consider a fluid element, initially at $(X_{-1/2}, Y_{-1/2})$, corresponding to $(r_0, \theta_{-1/2})$, which moves with the fluid surrounding it to $(X_{+1/2}, Y_{+1/2})$, corresponding to $(r_0, \theta_{+1/2})$ (see Figure 11b). Consequently, the measurement point at (X_0, Y_0) is no longer on the path followed by the fluid element. The components of the velocity field can be written as

$$V_{x,meas} = \frac{X_{+1/2} - X_{-1/2}}{\Delta t} = 0 \text{ and} \qquad (20)$$

$$V_{y,meas} = \frac{Y_{+1/2} - Y_{-1/2}}{\Delta t} = \frac{2r_0 \sin\left\{\omega(r_0)\frac{\Delta t}{2}\right\}}{\Delta t} \qquad (21)$$

The actual instantaneous velocity at the point (X_0, Y_0) can be written as

$$V_{x,act} = 0$$

$$V_{y,act} = r_0 \cos\left\{\omega(r_0)\frac{\Delta t}{2}\right\} \omega\left(r_0 \cos\left\{\omega(r_0)\frac{\Delta t}{2}\right\}\right) \qquad (22)$$

The difference between the actual velocity and measured velocity can be better assessed after

expanding both solutions as a power series and combining terms of the same order in Δt

$$\Delta V_x = 0$$

$$\Delta V_y = r_0 \omega(r_0)^2 \Delta t^2 \left\{\frac{1}{12}\omega(r_0) + \frac{1}{8}r_0\omega'(r_0)\right\} + \dots \qquad (23)$$

where ΔV_x and ΔV_y represent the bias error in each direction.

Using the central difference formulation for the velocity approximation, we would expect the

error in both velocity components to be on the order of Δt^2. However, there is *no error* in the

radial velocity component due to the azimuthal symmetry of the flow. The error in the azimuthal

component is order Δt^2 as expected.

Monte Carlo Simulations

One method for evaluating the accuracy of PIV algorithms is to process a set of simulated

particle images displaced according to a prescribed velocity field. This approach has certain

advantages over evaluating algorithms using experimental results, which will naturally have

errors and inaccuracies associated with them. Sets of simulated images can easily be constructed

for a variety of operating parameters by changing a few programming parameters. This

approach was used to assess the importance of operating parameters in the PIV process by Guezennec and Kiritsis (1990) and Keane and Adrian (1990) and many subsequent studies. Image pairs are simulated by creating a randomly distributed particle image field (hence the use of the term 'Monte Carlo') in the flow domain and then evolving the positions of those particles forward in time according to the prescribed velocity field; in this case Equation (15) above. Based on the observation of many real particle images, the particle image intensity can be modeled as a Gaussian curve. Because CCD cameras are composed of many small pixels, the Gaussian distribution of image intensities should be averaged over the area of each pixel as demonstrated by Huang, *et al.* (1997). While this step is very important when investigating the effect of subpixel resolution interpolation routines, it is not important in the current investigation because any imprecision in the particle image shape will be constant among the algorithms being evaluated.

In order to facilitate direct comparisons between the simulations and the experiments, the parameters of the simulations were closely matched to the experimental parameters. Even though the important parameters were matched, the simulated images were idealized in that all the particle images had the same diameter and the same intensity. All of the simulated particle images were set to the same maximal gray level intensity (107) that matched the mean particle brightness above the background level in the experiments. The background level of the simulations was set to be zero since the background only contributes to a DC component in the correlation plane. The mean particle image diameter (3.1 pixels) and the mean particle image concentration (3.3 particle images in a 16×16 pixel interrogation window) were also matched to typical experimental conditions. Twenty-six sets of image pairs were generated for each set of operating conditions explored.

Experimental Measurements

The experimental flow system, shown in Figure 12, consisted of two concentric acrylic cylinders, a rotating inner cylinder and a stationary outer cylinder with nominal radii r_i=4.24 cm and r_o=5.23 cm, respectively. The resulting gap width was d=r_o-r_i=0.99 cm, and the radius ratio was η= r_i/r_o=0.81. The inner cylinder was driven by a stepper motor at a rate of 0.106 Hz, below the transition to Taylor vortex flow. The stepper motor allowed the rotational speed to be precisely controlled. The actual rotation rate varied by ± 0.001 Hz which was monitored by an optical encoder having a resolution of 300 pulses per revolution. The two cylinders were held concentric by precision bearings mounted in opposing aluminum endcaps. The ratio of the length of the annulus to the gap width was Γ=47.8. The particles were illuminated by a laser light sheet formed in a plane perpendicular to the common axis of the cylinders and imaged through an acrylic window mounted in the lower endcap. The working fluid was a water-glycerine mixture, 40% by weight, with density 1.1 g cm^{-3} and viscosity 3.5 cSt at 21.5°C. The flow was seeded with 16 μm silvered hollow glass spheres having a density of 1.6 g cm^{-3}. The particles remained suspended due to their small size and have been shown to accurately follow the flow (Wereley and Lueptow, 1998).

Two 25 mJ per pulse Nd:YAG lasers operating at 20 Hz were used to illuminate the flow at consecutive time instants. The laser pulses were separated by 7.5, 15, 30, and 60 milliseconds, depending on the run, to study the dependence of the measurement error on the time step. The laser sheet had a thickness of approximately 1 mm, with ±0.5% variation in thickness in the measurement field. It was carefully aligned in a radial-azimuthal plane to avoid crosstalk between velocity components. Pairs of images each containing particle images from a single

laser flash were obtained using a TSI cross-correlation CCD camera, positioned perpendicular to the laser sheet. A Computar telecentric lens (model TEC-M55) with a 55 mm focal length and an aperture of f2.8 with 2X extender was used to avoid distortion caused by parallax. Twenty-six sets of image pairs, the same number of image sets generated in the Monte Carlo investigation, were recorded for each set of operating conditions explored.

Velocity Field Comparison

The sets of synthetic images produced through the Monte Carlo technique (discussed in Section 4.2) and the experimental images acquired (discussed in Section 4.3), were each analyzed twice. The first analysis was the forward difference interrogation, while the second was the central difference interrogation. While studying the convergence of the iterative, adaptive algorithms is not the primary purpose of the present work, it is certainly an important part of it. After each iteration is completed, the velocity produced from that iteration is used as the adaptive shifting file for the next iteration without alteration or correction. In general, the velocity data could be validated or smoothed at this point but that was not necessary for these measurements. After repeating this procedure several times, the measurement at a given point will either have reached a final value which does not change with subsequent iterations or it will be oscillating back and forth between two or more possible solutions. This oscillation is caused by the adaptive shift in one iteration leading to a measurement that does not produce the same shift in the next iteration. While this oscillation might at first seem troubling, it is very easy to explain and quantify. Figure 13 shows two measures of the convergence rate of the CDI algorithm as applied to the Taylor-Couette measurements here. The first measure is how quickly the RMS difference between the measured velocity and actual velocity approaches a final value and the second measure is the fraction of measurement points have *NOT* converged. Both of these measures are

plotted in Figure 13 as a function of iteration number. Both are also well-modeled by a decaying exponential which is superposed on each set of data point symbols. This figure demonstrates that with only a single iteration, the measurements are accurate to within 1% of the correct value, while after 3 iterations, the measurements are accurate to within 0.1%, and after 5 iterations, the measurements are accurate to within 0.02%, which is as accurate as they will ever get in these experiments. Figure 13 also shows that after 4 iterations, all but 1% of the measurements have reached a steady state value after which further iterations will produce no additional convergence. The iteration scheme used in this work is a very simple one, merely feeding back the velocity field produced in one iteration to calculate a more accurate velocity field in the next iteration, which worked adequately in this situation. A more robust approach would be to include some damping in each iteration to prevent the measurements from running away from the correct solution due to a bad measurement in one iteration and to prevent the oscillating measurements mentioned above. In addition, the fundamental assumption of PIV, that the particle images be randomly distributed, makes running away from the correct measurements statistically unlikely. As a safety check, any CDI measurement that differs from the FDI measurement made at the same point by more than some threshold amount can be replaced with the FDI measurement.

Because the experimental conditions did not exactly match the Monte-Carlo simulation conditions, the data are expressed as dimensionless quantities to facilitate comparisons between the two data sets. The radius ratio η was matched between the experiments and the simulations while the actual size (in pixels) of the inner and outer cylinders differed somewhat. For the simulations, the outer cylinder radius measured 890.0 pixels while for the experiments it measured 2316.1 pixels. Particle images were similarly larger in the experiments so that the

interrogation windows used in analyzing the experiments were square, measuring 16 pixels on a side, while for the simulations they were squares measuring 8 pixels on a side. The errors are expressed as fractional errors relative to the linear speed of the surface of the inner cylinder $v_{\theta,ic}$ since that is the only velocity scale available. The time delay between images Δt was expressed nondimensionally as the angular rotation measured in radians between the two laser flashes. Using these two dimensionless quantities, the radial velocity measurement error δv_r in the forward difference formulation expressed in Equation (19) can be rewritten as

$$\frac{\delta v_r}{v_{\theta,ic}} = -\frac{1}{2}\frac{v_\theta(r)}{v_\theta(r_{ic})}\cdot\omega(r)\Delta t = -\frac{1}{2}\Omega^*(r) \tag{24}$$

where $\delta v_r/v_{\theta,ic}$ is the fractional error and $\omega(r)$ angular rotation rate of the fluid at radius r which is given in Equation (15). $\Omega^*(r)$ is the modified angular displacement between laser flashes, measured in radians, of a fluid element at a radial position r. This modified angular displacement varies from zero at the outer cylinder to Ω_{ic} at the inner cylinder. In between the two cylinders, the modified angular displacement is scaled by the ratio of the local fluid velocity to the inner cylinder surface speed. From this relationship it is clear that the fractional error of the forward difference scheme will depend both on the radial position as well as on the time between laser flashes Δt. The parameter Ω^* can have several interpretations. It can be thought of as a dimensionless time step Δt because it is directly proportional to Δt for a fixed radial position. It can also be thought of as a dimensionless measure of radial position because it is a monotonic, albeit nonlinear, function of radial position when the time step Δt is fixed. Consequently it is an ideal parameter for comparing the experimental and computational results because it will allow both the effects of time step size as well as radial position to be explored.

To study the dependence of algorithm accuracy on increasing time delay lengths Δt, a succession of time delays and radial positions were studied. After the velocity fields were calculated for each data set, the Cartesian velocity vectors were decomposed into polar velocity vectors based on the location of the inner and outer cylinder walls. Any radial velocity component signifies an error because the flow should be purely azimuthal. The azimuthal error was found by subtracting the measured azimuthal component from that predicted by Equation (15). Since the azimuthal error is order Δt^2 for both algorithms, it does not provide any insight into which algorithm will be more effective and will not be discussed here. However, the radial error should be proportional to Δt as well as a function of radial position, as Equation 24 shows, for the forward difference algorithm while the error should not depend on the time delay for the central difference algorithm.

The dependence of the radial velocity error on radial position was explored first. The radial velocity component was divided by the surface speed of the inner cylinder and plotted as a function of both the parameter Ω^* (bottom axis) as well as the radial position (top axis) in Figure 14. For a fixed inner cylinder speed and the relatively large radius ratio of this experimental apparatus (η=0.81), the parameter Ω^* is nearly a linearly function of radial position with Ω^* equal to zero at the outer cylinder, a radial position equal to 1.00, and Ω^* equal to the angular displacement of the inner cylinder between laser flashes at the inner cylinder, a radial position equal to the radius ratio η=0.81. In Figure 14, each of the '+' symbols represents a single velocity measurement point while the solid line represents the predicted –1/2 slope line. The dashed lines represent one standard deviation ($\pm$0.0048) about the -1/2 slope line. The concentration of the symbols is greatest at the left side of the figure—the side of the figure that corresponds to the outer cylinder—and smallest at the right side of the figure—the side of the

figure that corresponds to the inner cylinder. Note that the symbols are not distributed all the way to the inner or outer cylinders because the finite size of the interrogation region excludes the centroids of the measurement points from reaching either wall. The concentration of measurement points varies significantly because of the area effect, i.e. larger radial positions correspond to larger areas containing more measurement points. The general sloping distribution of the measurement points confirms the prediction about how the error depends on radial position while the scatter in the measurement points (±0.0048) demonstrates the size of the random error in relation to the systematic bias error. Near the outer cylinder the random error dominates while near the inner cylinder the bias error dominates.

To quantify the bias error, i.e. radial velocity component, as a function of increasing time delays Δt, for each Δt the radial velocity measurements are plotted as a function of radial position (as in Figure 14) and a second order polynomial is fitted to the measurements to allow for curvature effects. The radial velocity that would be measured at the surface of the inner cylinder (where the bias error is worst) is calculated by finding the polynomial's value at the inner cylinder radial position. This quantity is plotted in Figure 15 as a function of angular displacement of the inner cylinder Ω^*. Figure 15 shows that for the forward difference interrogations of both the experimental images as well as the simulated images, the fractional errors calculated at each cylinder rotation Ω^* (dimensionless Δt) fall very near the predicted $-1/2$ slope line. Similarly, the central difference interrogations for both the experimental and simulated images are scattered about the predicted error of zero. We would expect these trends to continue until other error terms begin to dominate, such as the spatial gradients associated with larger inner cylinder rotations.

3. Application to Micronozzles

There is a significant effort in the aerospace community to miniaturize aircraft and spacecraft. In recent years, DARPA has focused resources on developing aircraft that are less than 13 cm in length. Miniaturized aircraft and spacecraft may potentially utilize a variety of microfluidic devices such as micro-turbines for power generation, microthrusters for thrust vectoring, and micronozzles for aerodynamic control.

Since the length scales of these devices are typically on the order of tens of microns, the Reynolds numbers that characterize these flows are several orders of magnitude lower than comparable devices at the macroscale. The Mach numbers associated with these microdevices are typically the same order of magnitude as their macroscopic counterparts. Relatively little attention has been focused on understanding flows with high Mach numbers and low Reynolds numbers. A notable exception is the work by Harley, *et al.* (1995) and others.

The next century of space exploration will emphasize the use of spacecraft that are less expensive, relatively simple, and significantly smaller in scale than current spacecraft (Tang, 1998). Advancements in microsystems technology will certainly play a role in the development of these new spacecraft. Microspacecraft require high precision thrust control for maneuvering and attitude control. For example, the thruster requirements for a 10 Kg spacecraft is to deliver impulse bits (I-bits) of 5 μN s with thrust levels of 1.8 mN. According to Tang [2], the World's smallest rocket engine is currently the *Moog 58x 125*, which delivers an I-bit of 100 μN s at the thrust level of 4.5 mN. To meet these design criteria, more precise microthrusters must be developed. Characteristically, cold gas thrusters produce lower impulse bits than what can be produced by more efficient thrusters such as resistojets and arcjets (Mueller, 1997).

Nearly all the supersonic nozzles that are currently used in spacecraft have been designed using inviscid flow calculations. However, at the microscale, Reynolds numbers are relatively low and viscosity effects cannot be neglected. The optimal nozzle shape and throat size for a specific thrust level remains unclear. Investigations of micronozzle performance have been limited to numerical simulations, or measurement of bulk flow properties (Mueller, 1997; Kim, 1994; Janson and Heelvajian, 1996; Bayt et al., 1997).

Bayt et al. (1997) fabricated micronozzles by Deep Reactive Ion Etching (DRIE) 2-D nozzle contours, entrance tanks, and exit tanks into 500 μm thick Silicon wafers. An example of this type of micronozzle is shown in Figure 16. The top and bottom of the Silicon wafers are anodically bonded to 500 μm thick glass wafers. Holes for fluid input and output are drilled into one of the glass wafers.

Micron Resolution Velocity Measurements

Until recently there has been no well-utilized technique for measuring the details of flow fields inside microfluidic devices. Meinhart et al. (199 gave a review of the available diagnostic techniques for microfluidics. Initial work in this area was conducted by Lanzillotto et al. [8]. They used x-ray micro-imaging to record the motion of $1 - 20$ μm emulsion droplets mixed in a liquid flow. The primary advantage of the x-ray technique is that it does not require optical access to image inside the microfluidic devices. However, it is limited to relatively slow flows and has relatively low spatial resolution.

The first successful micron-resolution PIV experiment was reported by Santiago et al. (1998). They used 300 nm dia. fluorescing flow-tracing particles to measure a steady Hele-Shaw flow around a 30 μm wide obstacle, with approximately 7 μm × 7 μm × 1.5 μm spatial resolution. Meinhart et al. (1999a) extended the technique, using a pair of Nd:YAG lasers to

illuminate 200 nm dia. fluorescing particles, to measure the flow through a 30 μm × 300 μm channel. A velocity-vector field measured in the microchannel is shown in Figure 3. The spatial resolution of the measurements were 13.8 μm × 0.9 μm × 1.8 μm. The velocity vectors were overlapped by 50%, yielding a velocity-vector spacing of 450 nm in the wall-normal direction.

The micro Particle Image Velocimetry (PIV) technique presented here is the first step towards measuring detailed flow fields inside micronozzles. There exist significant challenges that must be overcome in order to measure accurately velocity fields of high-speed flows at the microscale. These measurements will provide information about subsonic boundary layer growth, flow separation, and the streamwise evolution of the supersonic core flow.

Flow-Tracing Particles

The desire to measure high-speed velocity fields accurately inside micronozzles with order one-micron spatial resolution places significant constraints on the choice of flow-tracing particles. The particles must be significantly smaller than the length scale of the microdevice, and must be small enough to faithfully follow the flow under extremely large accelerations.

If a supersonic flow through a micronozzle accelerates from Mach 1 at the throat to Mach 2 one hundred microns downstream, and assuming uniform acceleration, the flow will accelerate at an average rate of approximately 9.0 E +08 m s^{-2}, or approximately 100 million times the acceleration of gravity. Assuming Stokes' drag, the difference between the particle velocity and the fluid velocity can be estimated by

$$|\mathbf{v} - \mathbf{u}| = \frac{\rho_p d_p^2 |\dot{\mathbf{v}}|}{36\rho\nu},$$

(25)

where $\mathbf{v}$ is the particle velocity, $\mathbf{u}$ is the velocity of the fluid, $\dot{\mathbf{v}}$ represents the total time derivative of the particle velocity, and the subscript p represents the properties of the particle

(Adrian, 1991). Using Silica (SiO_2), which has a density of 2 g cm^{-3}, a 100 nm dia. particle will slip $\sim$ 27 m s^{-1}, while a 50 nm dia. particle will slip $\sim$ 7 m s^{-1}. This represents about 4 – 8% FS error for the 100 nm and 1 – 2% FS error for 50 nm dia. particles. Under these conditions, a 100 nm dia. particle represents an upper bound on the size of particle that should be used for PIV measurements of high-speed flow in micronozzles.

The slip flow calculation from (25) assumes Stokes' drag is valid, which is a result of continuum flow theory. The mean-free path of N_2 at 10 atmospheres is approximately 8 nm, so the Knudsen numbers, $Kn = \lambda/d_p$, of the particles at the throat of the nozzle are approximately $Kn = 0.16$ and 0.08, for the 50 and 100 nm dia. particles, respectively. These Knudsen numbers are similar to Knudsen numbers of 0.5 – 1.0 μm dia. particles commonly used in PIV experiments of gaseous flows at standard laboratory conditions.

Flow-tracing particles must also be large enough to scatter sufficient light so that their images can be recorded. In the Rayleigh scattering regime, where the particle diameter is much smaller than the wavelength of light, $d_p \ll \lambda$, the amount of light scattered by a particle varies as d_p^{-6} (Born and Wolf, 1997). Since the diameter of the flow-tracing particles must not be larger than 50 nm – 100 nm, in order to follow the flow through supersonic nozzles, their diameters are 1/10 to 1/5 smaller than the wavelength of green light, $\lambda = 532$ nm, and are therefore approaching the Rayleigh scattering criteria. This places significant constraints on the image recording optics, making it extremely difficult to record particle images.

One solution to the imaging problem is to use epi-fluorescence imaging to record inelastically-scattered light from fluorescently-labeled particles through an optical filter, which removes the background light. This technique was used successfully in liquid flows to record images of 200 - 300 nm diameter fluorescent particles (Santiago *et al.*, 1998; Meinhart *et al.*,

1999a). While fluorescently-labeled particles are well suited for micro-PIV studies in liquid flows, they are not applicable to high-speed air flows for several reasons. First, commercially available fluorescently-labeled particles are available only in aqueous solutions. In principle, the particle-laden solutions can be dried, and the particles emitted into an air stream. Unfortunately, we have not been able to dry particles without significant particle clumping. Furthermore, the emission decay time of many fluorescent molecules is on the order of several nanoseconds, which may cause streaking of the particle images for high-speed flows. In contrast, elastic scattering is effectively instantaneous. Dry Silicate (SiO_2) particles are commercially available with diameters ranging between $50 - 100$ nm, and can be dispersed in air flows without significant clumping. Silicate particles have a density of 2 g cm^{-3}, which is about twice the density of polystyrene particles. Therefore, Silicate particles will slip twice the amount of polystyrene particles. Since the slip error is $\sim d_p^2$, the increase in error caused by using the denser Silicate particles, compared to the less-dense polystyrene particles, can be compensated by using a particle that is $\sqrt{2}$ smaller in diameter.

Spatial and Temporal Resolution

For the purposes of this discussion, we will define temporal resolution as the duration of averaging time required to obtain a measurement. In the case of double pulse PIV, the temporal resolution is simply the time delay between pulses, Δt. The ability to make accurate measurements while averaging over a short interval in time is important in variety of experiments. It is particularly important for measuring high-speed flows in micronozzle experiments. In this situation, the desire to make PIV measurements on the micron scale coupled with the large velocity associated with supersonic flows requires nanosecond temporal resolution.

Consider a flow near Mach 1 at standard temperature, with a characteristic velocity, $u_c = 340$ m s^{-1}. If the desired particle displacement is, say, $\Delta x \approx 10\mu$m, then the time delay between pulses should be, $\Delta t \approx 30$ ns. A standard *Nd:YAG* laser can be used to generate a short pulse of green light ($\lambda = 532$ nm), which is approximately Gaussian in time with a time duration, $\delta t \approx 5$ ns. During a 5 ns period, a particle with a characteristic velocity of $u_c = 340$ m s^{-1} travels approximately 1.7 µm. If a particle moves a significant fraction of its effective image size during exposure, the particle image will be blurred. In nearly all PIV experiments reported to date, the relatively short light pulse ($\delta t \approx 5$ ns) from an *Nd:YAG* laser is more than sufficient to freeze particle motion. It is only in the special case of high-speed microscale flow that the pulse duration of an *Nd:YAG* laser becomes limiting.

Further refinements in temporal resolution can be obtained by employing mode-locked *YAG* lasers or Titanium-Sapphire (*Ti-S*) lasers, which have pulse durations ranging between 50 fs - 100 ps. However for the current discussion, we will limit our investigation to standard *Nd:YAG* PIV lasers.

Following the arguments of Meinhart *et al.* [10] the diameter of the diffraction-limited particle image, d_s, can be approximated by

$$d_s = 2.44 M \frac{\lambda}{2\,\text{NA}},\tag{26}$$

where M is the magnification, and NA is the numerical aperture of the objective lens. Approximating the diffraction-limited image and the geometric image both as Gaussian functions one can estimate the effective diameter of a particle image as

$$d_e = \left[M^2 d_p^2 + d_s^2 \right]^{1/2}.\tag{27}$$

The blurred image resulting from a finite exposure time is the convolution of the instantaneous particle image function with the blurring function, where the blurring function, $B(X)$, can be written as

$$B(X) = \int \delta\left(X - X_p(t)\right) I(t)\, \sigma\, dt, \tag{28}$$

where X is the spatial coordinate on the CCD array, X_p is the centroid position of a particle when projected onto the CCD camera, δ is the Dirac delta function, I is the intensity of a the illuminating laser light pulse as a function of time, and σ is the scattering coefficient of the particles.

Since the intensity profile of the laser pulse is approximately Gaussian in time, the width of the blurred image due to the finite exposure time can be approximated by

$$d_{blur} = \left[d_e^2 + M^2 u_c^2 \delta t^2\right]^{1/2}, \tag{29}$$

The effective image diameter, d_e, of a 100 nm dia. particle imaged with a numerical aperture, NA = 0.6, 40x magnification objective lens, using $\lambda = 532$ nm light, is $d_e \sim 43$ μm. If the characteristic velocity is $u_c \sim 340$ m s^{-1}, and the duration of the laser pulse is $\delta t \sim 5$ ns, then the width of the blurred image is $d_{blur} \sim 80$ μm. When projected back into the fluid the width of the blurred image is ~ 2 μm. Assuming that one can measure the location of the particle to within 1/10th of width of the blurred image, then the uncertainty in determining the particle location is $\sim$ 200 nm. For a relative error of 2%, a particle image displacement of approximately 10 μm is required. This places a lower limit on the spatial resolution in the streamwise direction.

Differential Interference Contrast (DIC) Imaging

From the above discussions, it is clear that 50 – 100 nm dia. particles are required for accurate PIV measurements of high-speed flow in micronozzles. Moreover, the time duration of

an individual light pulse, and the time duration between light pulses must be $\delta t \leq 5$ ns and $\Delta t \sim 30$ ns, respectively. Since the emission decay time of most fluorescent molecules is on the order of several nanoseconds, and since it is difficult to seed fluorescently-dye sub-micron particles into air flow, we have chosen to work with $50 - 100$ nm dia. dry Silicate particles.

Transmitted Differential Interference Contrast (DIC) is a technique used in biological microscopy to image sub-cellular structures in transparent specimens, which are smaller or comparable to the diffraction resolution of the microscope. Reflective DIC is a microscopic technique used in Mineralogy to image extremely small features in non-transparent specimens. We have employed reflective DIC for the micronozzle experiments, because it requires optical access from only one direction.

The reflective DIC system shown in Figure 17 consists of a linear polarizer, a mirror, an adjustable Wollaston prism, and a DIC analyzer. The illumination light enters the system through the linear polarizer and is reflected by the mirror towards the Wollaston prism. The Wollaston prism consists of a birefringent material oriented at 45° to the incoming polarized light. The birefringence causes the incoming light to be sheared. The degree of beam shear is adjusted by sliding one element of the prism relative to the second element. It is common to adjust the shear so that it is less than the diffraction limit of the microscope so that a double image is not observed. The sheared beam illuminates the back of the objective lens, where it is refracted into the microfluidic device. Light is spectrally reflected from the surfaces of the microfluidic device, and scattered from the flow-tracing particles. The reflected light from the particles and the test section is collected by the objective lens and relayed through the Wollaston prism where the beam shear is reversed. Because optical systems are acausal, light waves that were relatively undisturbed in the test section will recover their original polarization, after reversing back

through the Wollaston prism. Light waves that have been phase shifted or changed in amplitude by objects that are of the same order in size as the beam shear will recover a different polarization, after reversing back through the Wollaston prism. The light is then relayed through the mirror onto a DIC analyzer. In the current configuration, the DIC analyzer is simply a linear polarizer oriented 90° to the incoming light. This filters out light that is relatively undisturbed in the test section over length scales on the order of the beam shear. In practice, the beam shear is adjusted to obtain maximum contrast for a particular type of object (Inoué and Spring, 1997).

The collected light is imaged onto a *Princeton Instruments* $1300 \times 1030 \times 12$ bit cooled CCD camera. A cooled CCD array is necessary to reduce electronic noise to a sufficiently low level to record light scattered from sub-micron particles. This particular camera was chosen because it has an interline-transfer array that can capture two back-to-back images within a 500 ns time duration. The time duration between pulses for the micronozzle experiments must be less than 100 nm. Therefore, both pulses of light must be recorded on the same camera frame.

Supersonic flow requires that the two light pulses be separated by $\Delta t \approx 30$ ns. The most common technique in PIV for producing two time-sequenced pulses is to use two separate lasers, which are synchronized by a high-precision electronic pulse generator. Pulse generators are commercially available with picosecond resolution. However, Nd:YAG lasers typically have a jitter of at least 1 ns.

An alternative method is proposed in Figure 17. It uses an optical delay to produce two time-sequenced pulses of light. The primary advantage of this technique is that the pulse sequence is highly repeatable, and not subject to electronic jitter. The primary disadvantage of this technique is that it is not easy to change the time delay and that the time delay cannot be set to the precision of digital electronics.

The proposed optical delay consists of a $\lambda/2$ waveplate that rotates the vertically polarized light emanating from the Nd:YAG laser to 45° angle. A polarizing beam splitter reflects the vertically polarized component of the light, and passes the horizontal component. Since the vertical component has a longer optical path, when the beams are recombine at the second beam splitter, the vertical component will be delayed relative to the horizontal component. A second $\lambda/2$ waveplate rotates the horizontally polarized and vertically polarized light pulses by 45°. Then a linear polarizer vertically polarizes both light pulses, so that they will be compatible with the DIC optics.

The ability of the DIC system to image 50 nm dia. Silicate particles using elastic scattering is demonstrated in Figure 18. A 3-D shadowing feature of the particle images is characteristic of DIC, and can be observed in Figure 18. Figure 18a shows images of 50 nm Silicate particles using a NA = 1.4 oil immersion 100x objective lens, while Figure 18b shows images of 50 nm Silicate particles using a NA = 0.6 air immersion 40x objective lens. The particles were not observable without the aid of DIC.

Since the 50 nm particles are much smaller than the diffraction resolution of the microscope, it is not clear initially that individual particles are being observed as opposed to clusters of particles. To answer this question, we took 50 nm fluorescently-dyed polystyrene particles. These particles were imaged using epi-fluorescence illumination. The same set of particles was then imaged using DIC. The epi-fluorescent technique utilizes purely in-elastic scattering while the DIC technique utilizes purely elastic scattering. Therefore, if a cluster of particles is imaged, the particle intensity resulting from epi-fluorescent imaging is proportional to the number of dye molecules being exposed, i.e. the number of particles in the cluster. On the other hand, the

particle intensity resulting from DIC imaging is related to the scattering coefficient of the particle cluster, which is a complicated function of the particle cluster geometry.

The intensity of the epi-fluorescent images has characteristic quantum levels, corresponding to a discrete number of particles in a specific cluster. Assuming the smallest increment between quantum levels corresponds to the fluorescence of a single particle, one can identify which clusters contain only a single particle. After single particle images are identified from the epi-fluorescence image, individual particle positions can be registered and images of single particles can be identified on the DIC image. This experiment demonstrates that we are imaging single 50 nm dia. particles using DIC (Matsumoto, 1999).

Velocity Measurements in a Micronozzle

The micronozzles used in the water-flow experiment were fabricated by Robert Bayt at MIT. The 2-D nozzle contours were etched using Deep Reactive Ion Etching (DRIE) in 300 μm thick Silicon wafers. The top and bottom of the wafers were anodically bonded to 500 μm thick glass wafers. Holes were then drilled into the glass to provide input and output fluid ports. The wafers are mounted to an aluminum manifold and sealed using O-rings and connected with plastic tubing to a *Harvard Apparatus* syringe pump.

The experiments were conducted using water as the fluid medium to determine the conditions in which PIV measurements could be obtained in the relatively deep micronozzles. The liquid flow was seeded with relatively large 700 nm dia. fluorescently-labeled polystyrene particles. The particles were imaged using a NA = 0.6, 40x objective lens, and an epi-fluorescent imaging system similar to that described by Meinhart *et al.* (1999a). A flow rate of 4 ml hr^{-1} was delivered to the nozzle by the syringe pump.

Figure 19 is an example of an instantaneous velocity field measured in the throat and expansion section of a straight diffuser with a 24° half angle. The velocity fields were calculated using a standard cross correlation algorithm. Both interrogation windows were 64×20 pixels in the x and y directions, respectively. When projecting into the fluid, the correlation windows were 10.9×3.4 µm in the x and y directions, respectively. The correlation windows were offset to the local particle-image displacement at each measurement point. The interrogation spots were overlapped by 50%, yielding a velocity-vector spacing of 5.44 µm in the streamwise direction and 1.7 µm in the spanwise direction.

The Reynolds number, based upon bulk velocity and throat width, is Re = 10, suggesting that nonlinear terms in the Navier-Stokes equation may be important in the expansion region of the nozzle. The PIV measurements reveal that the velocity profile is nearly parabolic in the throat. An inflection in the velocity profile is formed as the flow enters the expansion section. Further downstream in the expansion section, the flow separates from the lower nozzle wall. This suggests that separation may also occur for high-speed gas flows, where the Reynolds number can be two orders magnitude larger than the current experiment.

4. Extension to Air Flow

While the PIV technique has been demonstrated successfully by measuring liquid flows, the measurement of high-speed air flows through micronozzles remains difficult, in part because we would like to measure gas velocities and accelerations much higher than those measured in liquid flows. This translates into a requirement for particles of small size and mass, such that can faithfully follow the flow. Higher resolution in time will also be necessary to capture details of high-speed flow, as will shorter exposure times to prevent streaking. These requirements were discussed and quantified in Meinhart (1999c).

Imaging Solution: DIC

The optical method of Differential Interference Contrast (DIC) isproposed as a solution to the problem of imaging very small (50 – 100 nm) particles necessary for airflow PIV in micronozzles.

While DIC has been found to be quite successful in imaging small particles using white light, the use of DIC with laser illumination has not yet been optimized. Because of the coherence of the laser beam, a "laser speckle" diffraction pattern is produced when the DIC system is used with the Nd:YAG laser. There are various methods used to reduce laser speckle. Examples of these include: counter-rotating glass diffusers (Partlo, and Oldham, 1991), modified fiber array (Dingel, 1993), and illumination with a fluorescent beam produced by a laser dye.

Seeding the Gas Flow

In addition to the restrictions placed on the airflow PIV system by the higher speeds and accelerations, there is also the problem of seeding the flow, that is, developing and maintaining a

sufficiently disperse aerosol of solid or liquid particles in the gas stream. There are at least four commonly used methods for suspending such an aerosol.

A powder disperser uses a gas stream, either aimed at a powder sample or bubbled up through the powder to create a powder cloud, or blown through a venturi to suck powder up into the throat. The particles dispersed in the gas stream are normally clumps of several individual particles (Melling, 1997); indeed it is very difficult to distribute a completely deagglomerated aerosol. Reducing moisture in the gas stream and in the powder sample may help in dispersion efficiency by reducing hydrostatic coagulation forces, but this must be balanced with the effect of electrostatic forces, which increase with dryness (Melling). Particle size and material also play a part in agglomeration. TSI (St.Paul, MN) quotes their powder dispersers as able to disperse powders larger than 500 nm; anything smaller is not effectively deagglomerated. Rough, soft particles are more difficult to disperse than smooth, hard particles (Melling, 1997).

An atomizer avoids the problem of deagglomerating cohesive powders. A pressure difference across a nozzle pulls liquid through the nozzle, creating a polydisperse liquid aerosol. If the liquid is a suspension of (monodisperse) solid particles, the aerosol can be dried, leaving a (monodisperse) dilute aerosol of solid particles. Alternatively, if the liquid is a solution (saline is common), the aerosol can be dried, leaving a solid aerosol of solute crystals.

A condensation aerosol generator allows a vaporized medium to condense on a tiny nucleus. If this is done at constant temperature, as in a Sinclair-LaMer type generator, a monodisperse aerosol is attained, though it is relatively low in concentration.

An electrospray aerosol generator, such as the one developed by TSI, Inc., uses an electric field to pull uniform tiny liquid droplets off the end of a capillary tube. The resulting aerosol is monodisperse and nearly comparable in concentration to that of the atomizer, the droplet size is

150 nm. If these droplets are a saline solution, final solid particle size can be as large as 50-100 nm. While this coincides with the ideal size for airflow seeding particles, it is necessary to be able to produce larger (easily seen) particles as well during the optimization of the imaging and flow systems.

Coagulation

As soon the aerosol is generated, it unfortunately begins to recoagulate. As particles move relative to each other by Brownian motion, turbulence, or body forces, they collide and coalesce. Theoretical treatments of coagulation begin by assuming perfect collision efficiency, that is any particles which come into contact will stick (Green, 1964, Fuchs, 1964, and Reist, 1993 all present details on coagulation.) If particles that collide do not stick together, they will, because of proximity, have an increased probability of another collision, thus raising the "effective" collision efficiency. If a monodisperse aerosol is moving only through Brownian motion, the number concentration n as a function of time may be described as

$$\frac{1}{n} = \frac{1}{n_o} + Kt \tag{30}$$

where K is the coagulation constant. K can be derived theoretically for the above case, and turns out to be 4.0×10^{-10} cm^3/s for 200 nm particles in air at STP (Fuchs, 1964), but additional complications of our system such as polydispersity and turbulence, may affect this number by orders of magnitude. Nevertheless, some interesting observations may be made about this process. First, for a high coagulation constant, and an observation point a finite time after $t = 0$ (tenths of seconds perhaps), increasing the initial concentration is meaningless: the particles will immediately coagulate. There is therefore, a limit to the concentration of an aerosol that can be

generated and maintained. Second, for high initial concentrations, it is important for the observation point to be as soon as possible after $t = 0$ so as not to allow the aerosol to coagulate. This translates for us into a short as possible run between the aerosol generator and the test section. We keep these practical limitations in mind as we search for a flow seeding method.

Airflow Velocimetry Experiments

Although it is common to use aerosol generators of the aforementioned type for seeding gas flow for PIV, most experiments have been done on much larger scale. A reduction in scale not only necessitates a reduction in particle size, but also an increase in particle number concentration. Our needs, therefore, push the limits of what has been used, what is available, and perhaps what is possible. If a 40X, N.A. 0.6 objective lens is used, depth of field, taken from Meinhart *et al.* (2000a), is 10 μm, and resolution of the camera is taken to be 6.8 μm / pixel, the image volume is 3.74×10^{-7} cm^3. If 15 particles are needed per interrogation volume and interrogation windows of 64 X 20 pixels are used as in Meinhart (1999c) corresponding to a resolution of 5.44 X 1.7 μm, then it is desirable to have about 4.5×10^5 particles per image volume. Ensemble averaging techniques for steady flow can reduce this nearly an order of magnitude (Meinhart *et al.*, 1999b), but that still leaves a desirable aerosol concentration of 2×10^{10} particles / cm^3. Specified maximum number concentrations on commercially available aerosol generators run in the 10^6 to 10^8 range, so dispersion of a highly concentrated aerosol becomes one of the limiting system criteria.

Shallow Channel Design

In order to ignore for the moment the problems associated with high speed flow, and to increase the overall volume flow rate, which generally increases aerosol generation, a new channel was designed for testing the airflow PIV system, shown in Figure 20. The channel is

wide, increasing the flow rate, and shallow, keeping the illuminated depth to a minimum to reduce noise from out-of-focus particles. Additionally, because the channel is quickly made on a mill rather than using micromachining techniques, there is more flexibility than with the micronozzle. For example, the bottom of the channel was colored black to improve image quality. In another design, the channel and manifold were made from acrylic, to allow illumination from behind the channel. The intent is to use the less restrictive shallow channel to get a PIV system working. The system can then be fine-tuned for the more restrictive micronozzle.
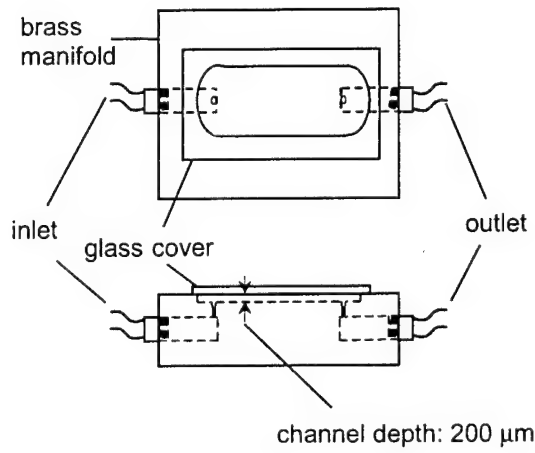
Figure 20. Shallow Channel Design
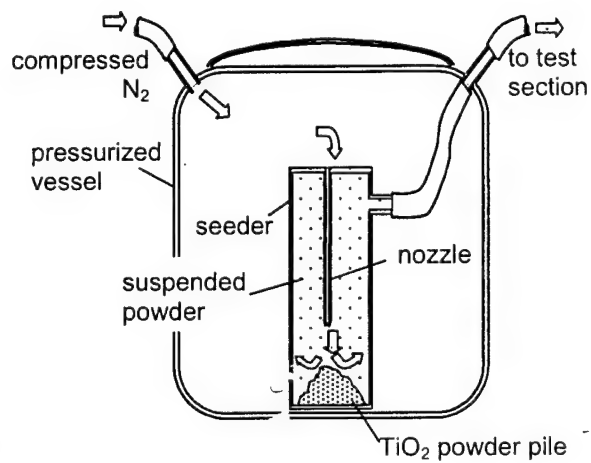
Figure 21. Powder Dispersion Seeder

Powder Dispersion Seeder

The first aerosol generation system used was a powder dispersion seeder designed and built in-house, diagrammed in Figure 21. Nitrogen is the working gas; TiO_2 was chosen as the powder because of its availability in a range of appropriate sizes and its low density (compared with metals). A gas stream impinges on a pile of powder, creating a cloud of powder. The pressure

differential between the cloud chamber and the outside causes the cloud to be sucked through the channel.

This seeder was not effective in producing observable particles in the flow stream. Because there was clearly powder exiting the test section, the absence of particles in any images could be traced to either of two problems: first, the imaging system was not capable of detecting such small particles; or second, the seeder was distributing such a low concentration (and given the observed powder mass flow, large particle size) of particles, the chances of one falling in the exposure window were quite low. Because various sizes of TiO_2 particles were used (200 – 700 nm average diameter), which were easily imaged when captured on a glass slide, and because finally one large (~5 μm) particle entrained in the flow was captured in an image, it seems more logical that the problem is with the agglomeration of the powder and therefore the low number concentration of the aerosol. There was also obvious loss of aerosol to tubing walls, which were coated with powder at the end of each experiment. Special conductive flexible tubing was tried, with no measured improvement in results.

Atomizer

A TSI, Inc. Atomizer (Model 3076) was used in the airflow velocimetry system. Using simply water as a working liquid, an aerosol of water droplets was produced. The shallow channel quickly became waterlogged, that is, enough water quickly deposited on the viewing window so as to prevent imaging. Therefore, for evaluation of the atomizer as an aerosol generator, the channel was removed, and the flow was simply aimed at a glass slide through which the flow was observed. In this configuration, a droplet was captured in an image about every third frame. From this, an aerosol concentration can be inferred of around 10^5 particles/cc

of particles larger than the smallest detectable size. TSI's specifications for this instrument quote 10^8 particles/cc with a mean diameter of 3.0 μm and a geometric standard deviation of less than 2.0. From the image pairs gathered of the droplets in external flow, a uniform velocity of 1.2 m/s was calculated.

References

Adrian, R. J. 1988. Double Exposure, Multiple-field particle image velocimetry for turbulent probability density. *Optics and Lasers in Eng.*, Vol. **9**, pp. 211-228.

Adrian RJ 1991 Particle-imaging techniques for experimental fluid mechanics. *Annu. Rev. Fluid Mech*, Vol. 23, pp. 261-304.

Adrian, R. J. & Yao, C. S. 1985. Pulsed laser technique application to liquid and gaseous flows and the scattering power of seed materials. *App. Optics*, Vol. 24, No. 1, pp. 44 – 52.

Agui, J. and Jimenez, J., 1987, 'On the Performance of Particle Tracking,' *J. Fluid Mech.*, **Vol. 186**, pp. 447-468.

Bayt, R. L., Ayon, A. A., Breuer, K. S. 1997. A performance evaluation of MEMS-bases micronozzles. *AIAA Paper 97-3169, 33rd AIAA/ASME/SAE/ASEE Joint Propulsion Conference & Exhibit*, July 7-9, Seattle, WA.

Born, M & Wolf E 1997. Principles of Optics. *Pergamon Press*.

Cohn, R. K. and Koochesfahani, M. M., 1999, 'The Accuracy of Remapping Irregularly Spaced Velocity Data onto a Regular Grid and the Computation of Vorticity,' pp. 225-230, Third International Workshop on Particle Image Velocimetry, Santa Barbara, CA, Sept. 1999.

Cowen, E. A. and Monismith, S. G., 1997, 'A hybrid digital particle tracking velocimetry technique,' *Exp. Fluids*, **Vol. 22**, pp. 199-211.

Crenshaw, H 1998. *Personal Communication*.

Dingel, B., Kawata, S. & Minami, S. 1993. Speckle reduction with virtual incoherent laser illumination using a modified fiber array. *Optik.* **Vol. 94**, pp. 132-136.

Dudgeon and Mersereau, 1984, *Multidimensional Digital Signal Processing*, Prentice-Hall.

Fuchs, N. A. 1964. *The Mechanics of Aerosols*. Pergamon Press, New York.

Green, H. L. and Lane, W.R. 1964. *Particulate Clouds: Dusts, Smokes and Mists, 2nd ed.* E. & F. N. Spon Ltd., London.

Guezennec, Y.G. and Kiritsis, N., 1990, 'Statistical investigation of errors in particle image velocimetry,' *Exp. Fluids*, **Vol. 10**, pp. 138-146.

Harley, J. C, Huang, Y., Bau, H. H. & Zemel, J. N. 1995. Gas flow in micro-channels. J. *Fluid Mech.* **Vol. 284**, pp. 257-274.

Huang, H., Dabiri, D., and Gharib, M., 1997, 'On errors of digital particle image velocimetry,' *Meas. Sci. Technol.*, **Vol. 8**, pp. 1427-40.

Inoué, S & Spring, KR 1997. Video Microscopy, Second Edition, *Plenum Press*.

Janson, S.W. & Helvajian, H. 1996. Batch-fabricated microthrusters: initial results. *AIAA Paper No. 96-2988*.Keane, R. D. & Adrian, R. J. 1991. Optimization of particle image velocimeters. II. Multiple pulsed systems. *Meas. Sci. & Tech.*, Vol.2, No.10, Oct. 1991. pp. 963 - 974.

Keane, R. D., Adrian, R. J., 1990, 'Super-resolution particle imaging velocimetry,' *Meas. Sci. Tech.* **Vol. 1**, pp. 1202-1215.

Keane, R. D. & Adrian, R. J. 1992. Theory of cross-correlation analysis of PIV images. *App. Sci. Res.*, **Vol. 49**, pp. 191-215.

Keane, R. D., Adrian, R. J., 1993, 'Theory and Simulation of Particle Image Velocimetry,' *Proc. SPIE*, **Vol. 2052** (Laser Anemometry Advances and Applications. Fifth International Conference, Veldhoven, Netherlands, 23-27 Aug. 1993), p.477-92.

Kerker, M 1969. The scattering of light. *Academic Press*.

Kim, S. C. 1994. Calculations of low-Reynolds number resistojet nozzles. *J. Spacecraft and Rockets*, **Vol. 31,** No. 2.

Lanzillotto, A. M., Leu, T. S., Amabile, M., Wildes, R. and Dunsmuir, J. 1996. Applications of x-ray micro-imaging, visualization and motion analysis techniques to fluidic microsystems. *Proceedings from Solid-state sensors and actuators workshop*, Hilton Head, SC, June 13-16.

Lourenco, L. and Krothapalli, A., 1998, 'Mesh-free second order accurate algorithm for PIV processing,' *Proc. of Int. Conf. on Optical Technology and Image Processing in Fluid Thermal and Comb. Flow*, Yokohama, Japan.

Matsumoto B. 1999. *Personal Communication.*

Meinhart, CD, Prasad, AK & Adrian, RJ 1993. A parallel digital processor for particle image velocimetry. *Measurement Science Technology*, **Vol. 4**, pp. 619-626.

Meinhart, C. D., Barnhart, D. H. & R. J. Adrian 1994. Interrogation and validation of three-dimensional vector fields. In Developments in Laser Techniques and Applications to Fluid Mechanics, R. J. Adrian *et al.* (Eds.), Springer-Verlag, Berlin, pp. 379-391.

Meinhart, C. D. & Adrian, R. J. 1995. On the existence of uniform momentum zones in a turbulent boundary layer. *Phys. Fluids*, **Vol. 7** No.4, pp. 694-696

Meinhart, C. D., Wereley, S. T. & Santiago, J. G. 1999a. PIV Measurements of a Microchannel

Flow. *Exp. in Fluids* **Vol. 27**, pp.414-419.

Meinhart, C. D., Wereley, S. T. & Santiago, J. G. 1999b. A PIV Algorithm for Estimating Time-Averaged Velocity Fields. *Proceedings of Optical Methods and Image Processing in Fluid Flow, 3rd ASME / JSME Fluids Engineering Conference,* July 18-23, San Francisco, CA.

Meinhart, C. D., Gray, M. H. B. & Wereley, S. T.,1999c. PIV measurements of high-speed flows in silicon-micromachined nozzles. American Institute of Aeronautics and Astronautics, AIAA-99-3756

Meinhart, C. D., Wereley, S. T., & Santiago. J. G. 1999d Micron-Resolution Velocimetry Techniques. In *Developments in Laser Techniques and Applications to Fluid Mechanics*, R. J. Adrian *et al*. (Eds.), Springer-Verlag, Berlin.

Meinhart, C. D., Wereley, S. T. & Gray, M. H. B. 2000a. Volume illumination for two-dimensional particle image velocimetry. *Meas. Sci. Technol.* **Vol. 11,** pp. 809-814.

Meinhart, C.D., Wereley, S.T., and Santiago, J.G., 2000b, 'A PIV Algorithm for Estimating Time-Averaged Velocity Fields,' *J. Fluids Eng.*, **Vol. 122**, 285-289.

Mueller, J. Thruster Options for Microspacecraft: A Review and Evaluation of Existing Hardware and Emerging Technologies. *AIAA 97-3058, 33rd AIAA/ASME/SAW/ASEE Joint Propulsion Conference and Exhibit*, July 6-9, 1997, Seattle, WA.

Prasad AK; Adrian RJ; Landreth CC, Offutt PW 1992. Effect of resolution on the speed and accuracy of particle image velocimetry interrogation. *Exp Fluids* 13: 105-116

Melling, A. 1997. Tracer particles and seeding for particle image velocimetry. *Meas: Sci. Technol.* **Vol. 8**, pp. 1406-1416.Santiago, JG, Wereley, ST, Meinhart, CD, Beebe, DJ & Adrian, RJ 1998.A micro particle image velocimetry system. *Exp. Fluids*, Vol. 25 No.4, pp 316-319.

Partlo, W. N. and Oldham, W. J. 1991. Reducing coherence in a fith-harmonic YAG source (213 nm) for use in microlithography. *J. Vac. Sci. Technol. B*. **Vol. 9**, pp. 3126-3131

Reist, P. C. 1993. *Aerosol Science and Technology, 2nd ed*. McGraw Hill, New York.

Santiago, J. G., Wereley, S. T., Meinhart, C. D., Beebe, D. J., and Adrian, R. J., 1998, 'A Particle Image Velocimetry System for Microfluidics,' *Exp. Fluids*, **Vol. 25**:4, pp.316-19.

Sobek, D, Senturia, SD, and Gray, ML 1994. Microfabricated fused silica flow chambers for flow cytometry. *Proceedings from Solid-State Sensors and Actuators Workshop*, Hilton Head, SC, June 13-16.

Santiago, J. G., Wereley, S. T., Meinhart, C. D., Beebe, D. J. & Adrian, R. J. 1998. A micro particle image velocimetry system. *Exp. Fluids*, Vol. 25 No.4, pp 316-319.Spedding, G. R. and Rignot, E. J. M., 1993, 'Performance Analysis and Application of Grid Interpolation Techniques for Fluid Flows,' *Exp. Fluids*, **Vol. 15**, pp. 417-430.

Tang, W. C. 1998. Micromechanical Devices at JPL for Space Exploration, *IEEE Aerospace Conference*, Snowmass, CO.Tieu, A. K., Mackenzie, M. R., Li, E. B. 1995. Measurements in microscopic flow with a solid-state LDA. *Exp. Fluids*, **Vol. 19**, pp. 293 – 294.

Urushihara, T., Meinhart, C. D. & Adrian, R. J., 1993, 'Investigation of the logarithmic layer in pipe flow using particle image velocimetry,' In *Near-Wall Turbulent Flows*, R. So, *et al.* (Eds.), New York: Elsevier, pp. 433-46.

Westerweel, J., 1993, 'Analysis of PIV interrogation with low-pixel resolution,' *Proc. SPIE*, **Vol. 2005,** pp. 624-635.

Westerweel, J. 1993. Efficient detection of spurious vectors in particle image velocimetry data. *Exp. Fluids*, **Vol. 16**, pp. 236 – 247.

Westerweel, J., Draad, A. A., van der Hoeven, J. G. Th. & van Oord, J. 1996. Measurement of fully developed turbulent pipe flow with digital PIV. *Exp. Fluids*. Vol. 20, pp. 165 – 177.

Westerweel, J. 1997. Fundamentals of digital particle image velocimetry. *Meas. Sci. Technol.* **Vol. 8,** pp. 1379 – 1392.

Wereley, S.T. and Lueptow, R.M., 1994, "Azimuthal velocity in supercritical circular Couette flow," *Exp. Fluids*, **Vol. 18**, pp. 1-9.

Wereley, S.T. and Lueptow, R.M., 1998, "Spatio-temporal character of nonwavy and wavy Taylor Couette flow," *J. Fluid Mech.,* **Vol. 364**, 59-80.

Wereley S.T., Meinhart, C.D., Santiago, J.G., and Adrian, R.J., 1998, "Velocimetry for MEMS Applications," *Proc. ASME/DSC*, **Vol. 66**, 453-459, (Micro-fluidics Symposium, Anaheim, CA, Nov. 1998).
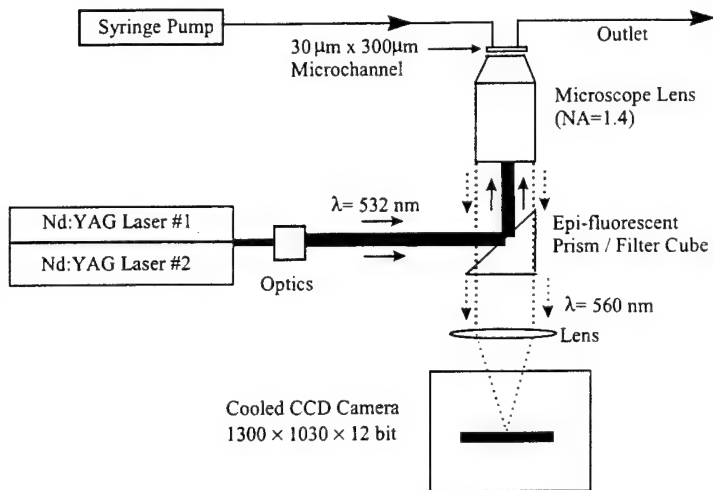
Figure 1. Schematic of a micro PIV system. A pulsed Nd:YAG laser is used to illuminate 200 nm diameter fluorescent flow-tracing particles through an epi-fluorescent inverted microscope. A cooled 1300 × 1030 pixel × 12 bit interline-transfer CCD camera is used to record the particle images.
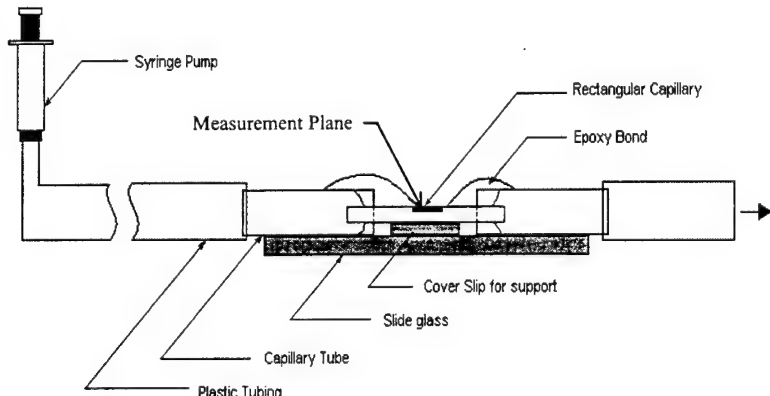
Figure 2. Detail of the nominally 30 μm × 300 μm rectangular glass microchannel, which is glued to a circular capillary tube and a 170 μm glass coverslip for support. Plastic tubing connects the capillary tube to the syringe pump.

(a)
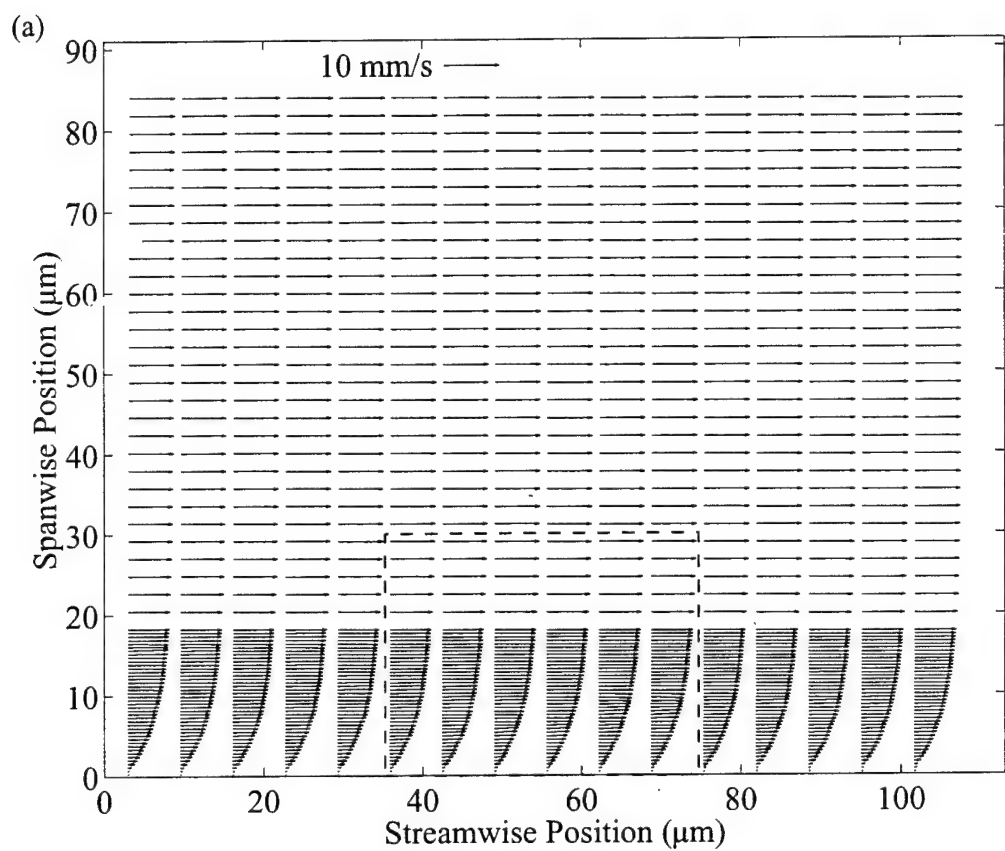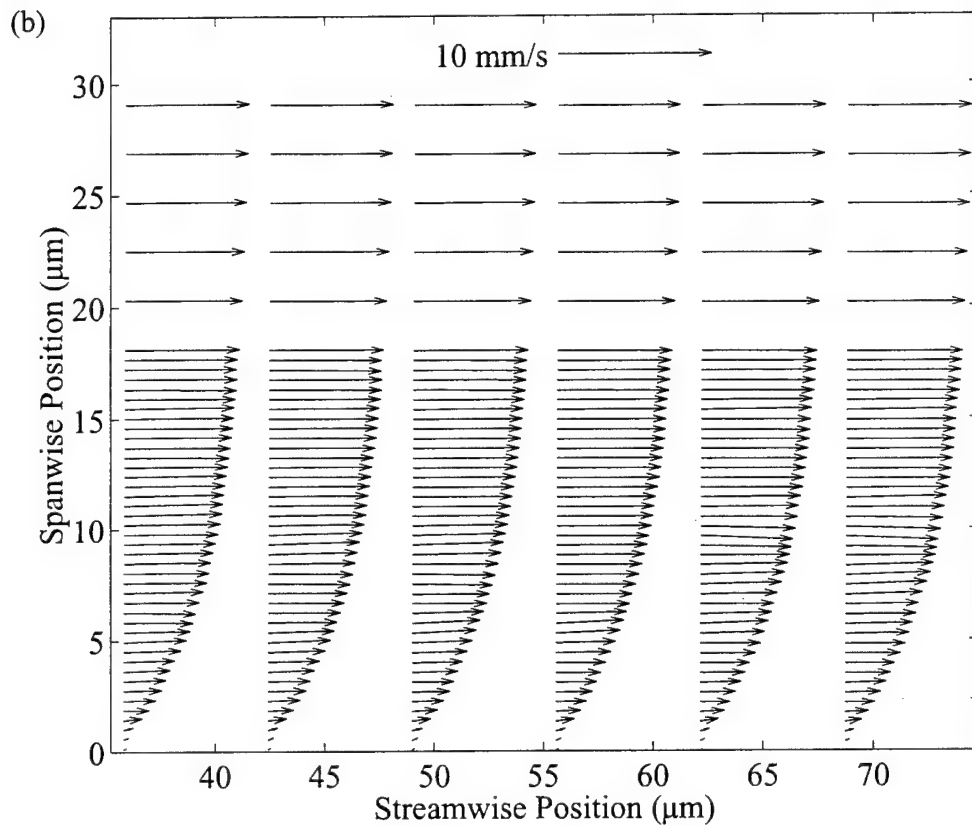
Figure 3. Ensemble-averaged velocity-vector field measured in a 30 μm deep × 300 μm wide × 25 mm channel. The spatial resolution, defined by the interrogation spot size of the first interrogation window, is 13.6 μm × 4.4 μm away from the wall, and 13.6 μm × 0.9 μm near the wall. A 50% overlap between interrogation spots yields a velocity vector spacing of 450 nm in the wall-normal direction near the wall: (a) large-scale vector field showing a 100 μm × 85 μm cross section of the channel, (b) near-wall view of the lower 30 μm of vector field.
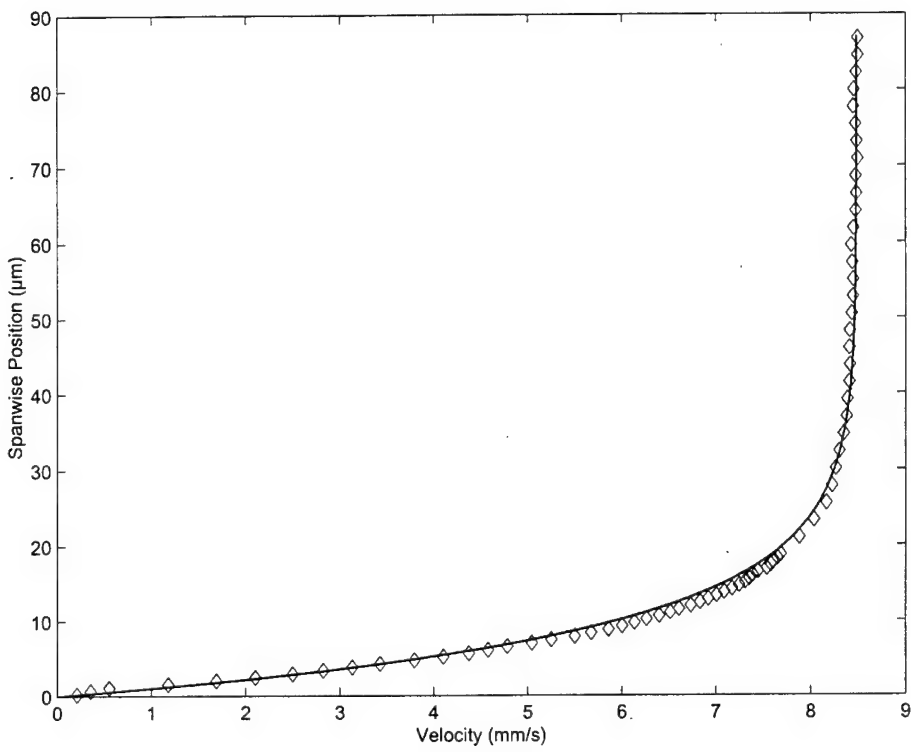
Figure 4. Ensemble-averaged velocity profile measured in a nominally 30 μm × 300 μm channel. The symbols represent ensemble-averaged and streamwise-averaged PIV data. The solid line is the analytical solution for Newtonian flow through a rectangular channel.
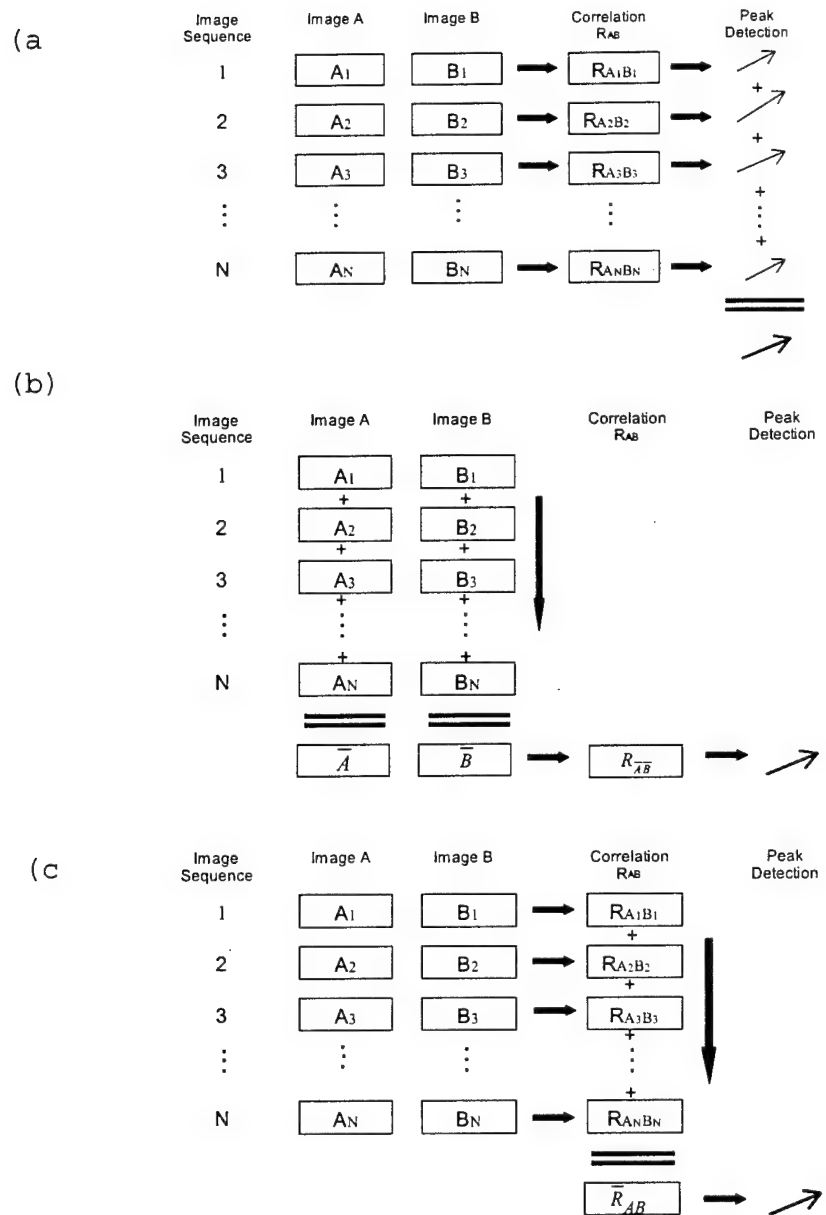
Figure 5. Diagrams depicting the different ways in which the average velocity can be estimated: (a) average velocity method, (b) average image method, (c) average correlation method.
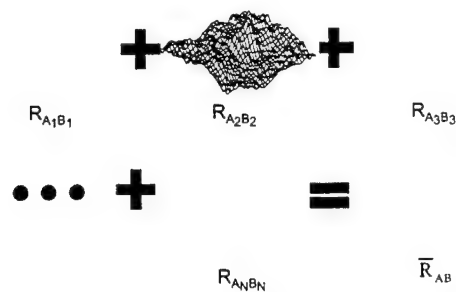
Figure 6. Instantaneous cross correlation functions that are averaged together to produce an average correlation function. The average correlation function has a much higher signal-to-noise ratio than the instantaneous correlation functions.

(a)

Streamwise Position (μm)
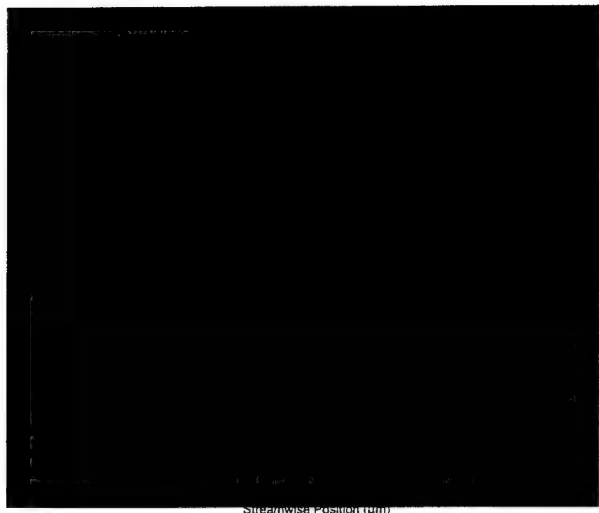
(b)
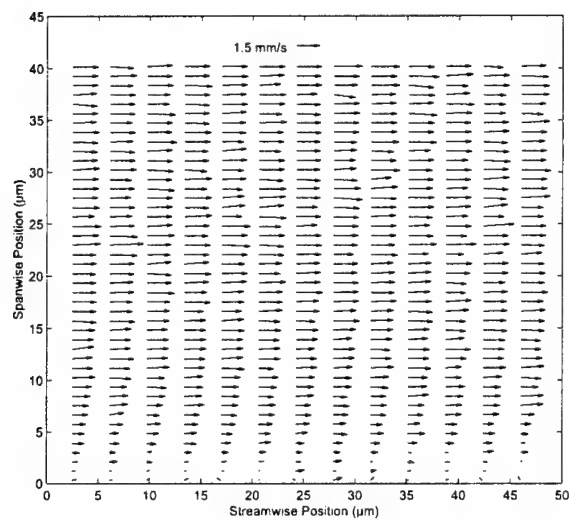
(c)
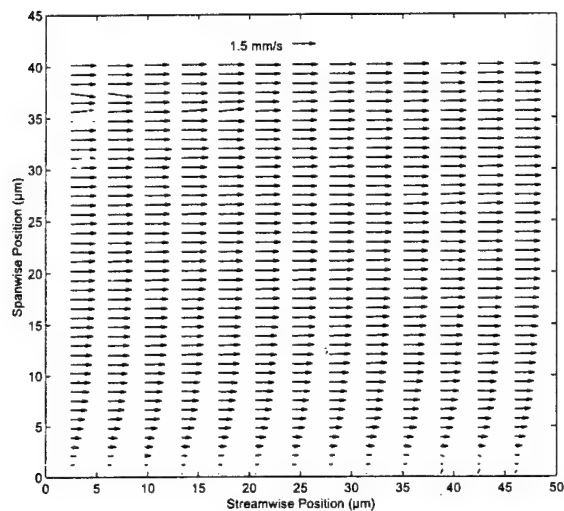
Figure 7. Velocity vector fields showing the results from the different methods of calculation: (a) Instantaneous velocity field, (b) time average of twenty instantaneous velocity fields, (c) velocity field calculated from the time average of twenty correlation functions.
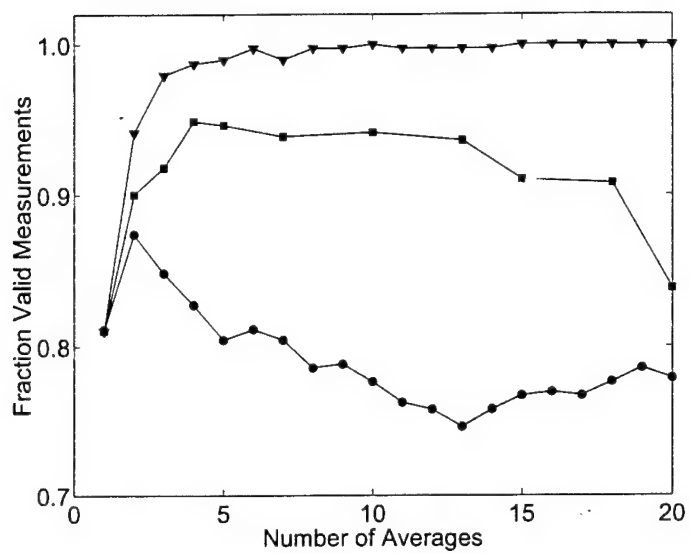
Figure 8. Comparison of the performance of the three averaging techniques: average velocity •, average image ■, and average correlation ▼.
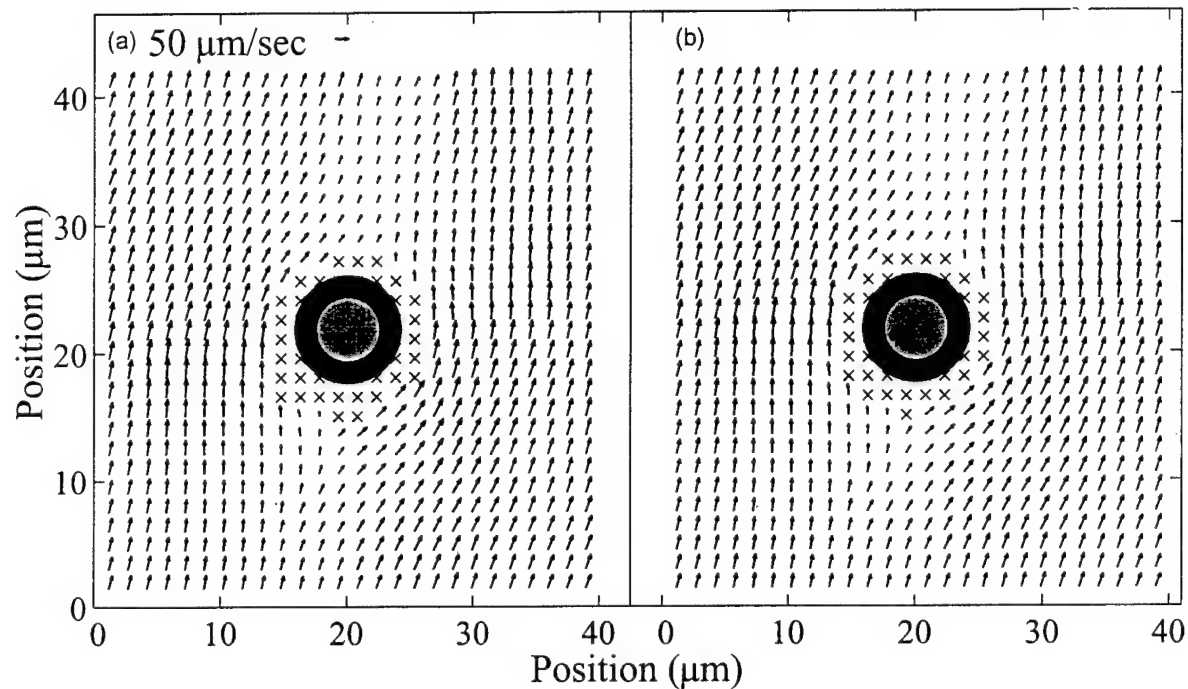
Figure 9. Comparison of a forward difference adaptive window offset analysis (a) vers·is a central difference adaptive window offset analysis (b) of the flow around a single red blood cell. This figure demonstrates quantitatively the advantage of using the second order central difference interrogation (CDI) scheme.
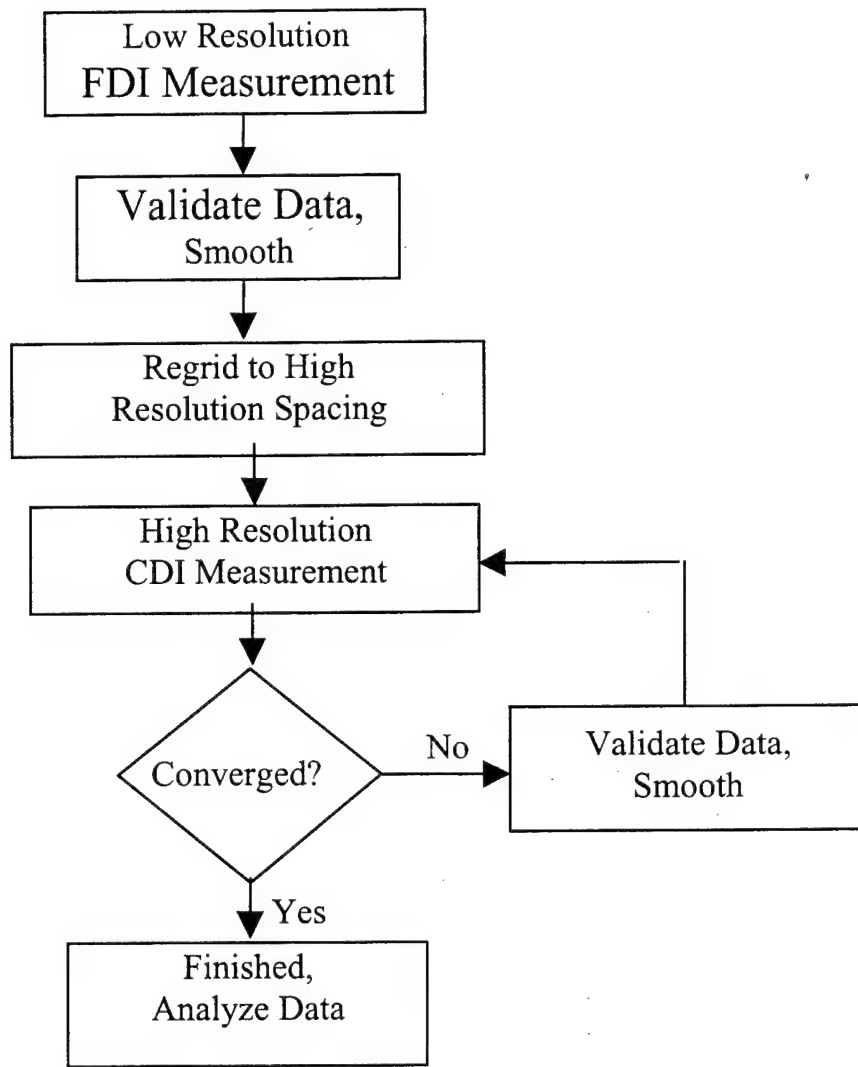
Figure 10. Flowchart demonstrating iterative procedure necessary adaptive image shifting and second order accuracy.
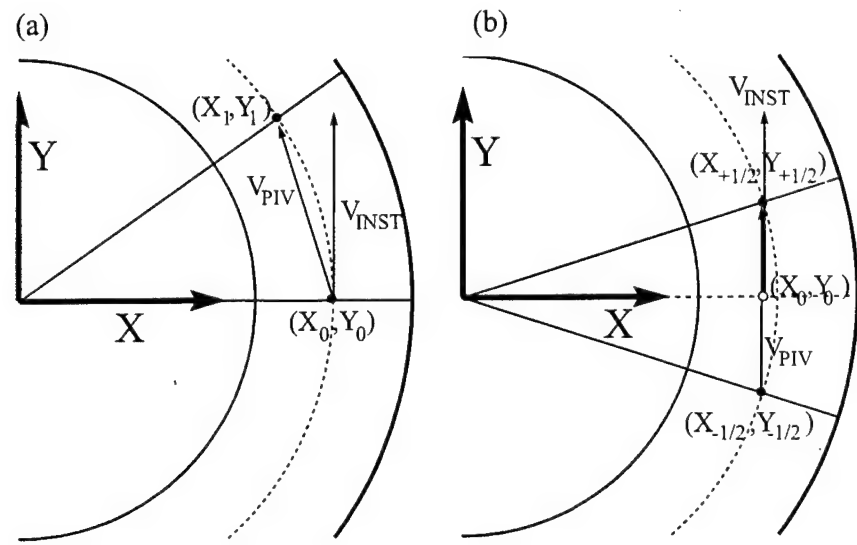
Figure 11. Schematic views illustrating the (a) forward difference interrogation algorithm and the (b) central difference interrogation algorithm as applied to the cylindrical Couette flow system. The dashed squares represent spatially offset interrogation regions while the dashed circles represent the path that a fluid element would follow.
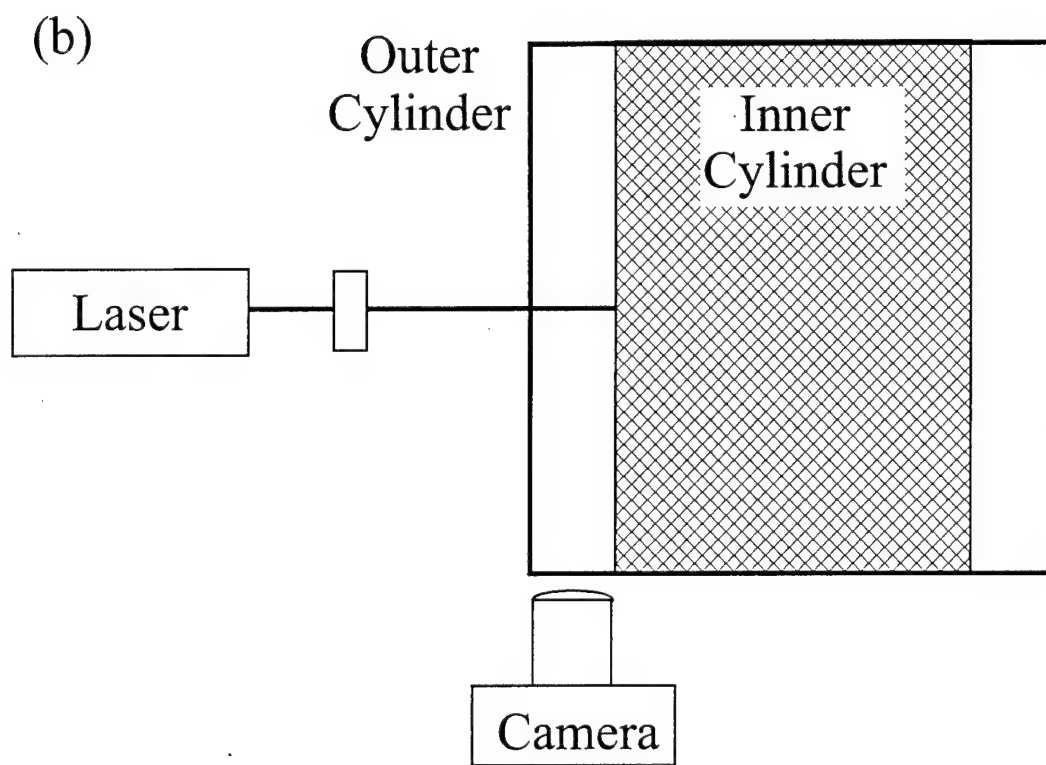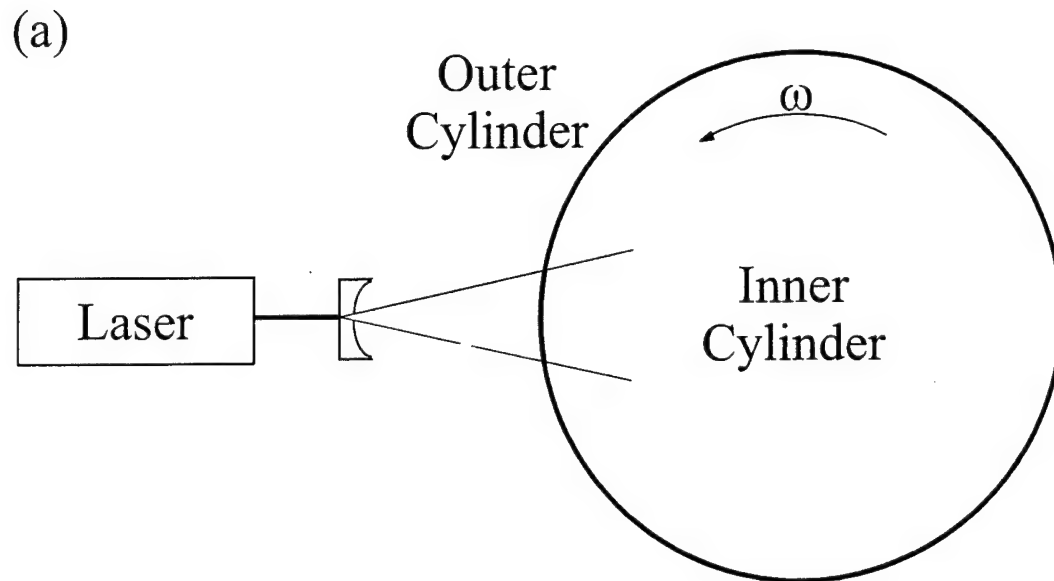
Figure 12. Experimental setup. The camera-light sheet orientation indicates that velocity components in a radial-azimuthal plane will be measured.
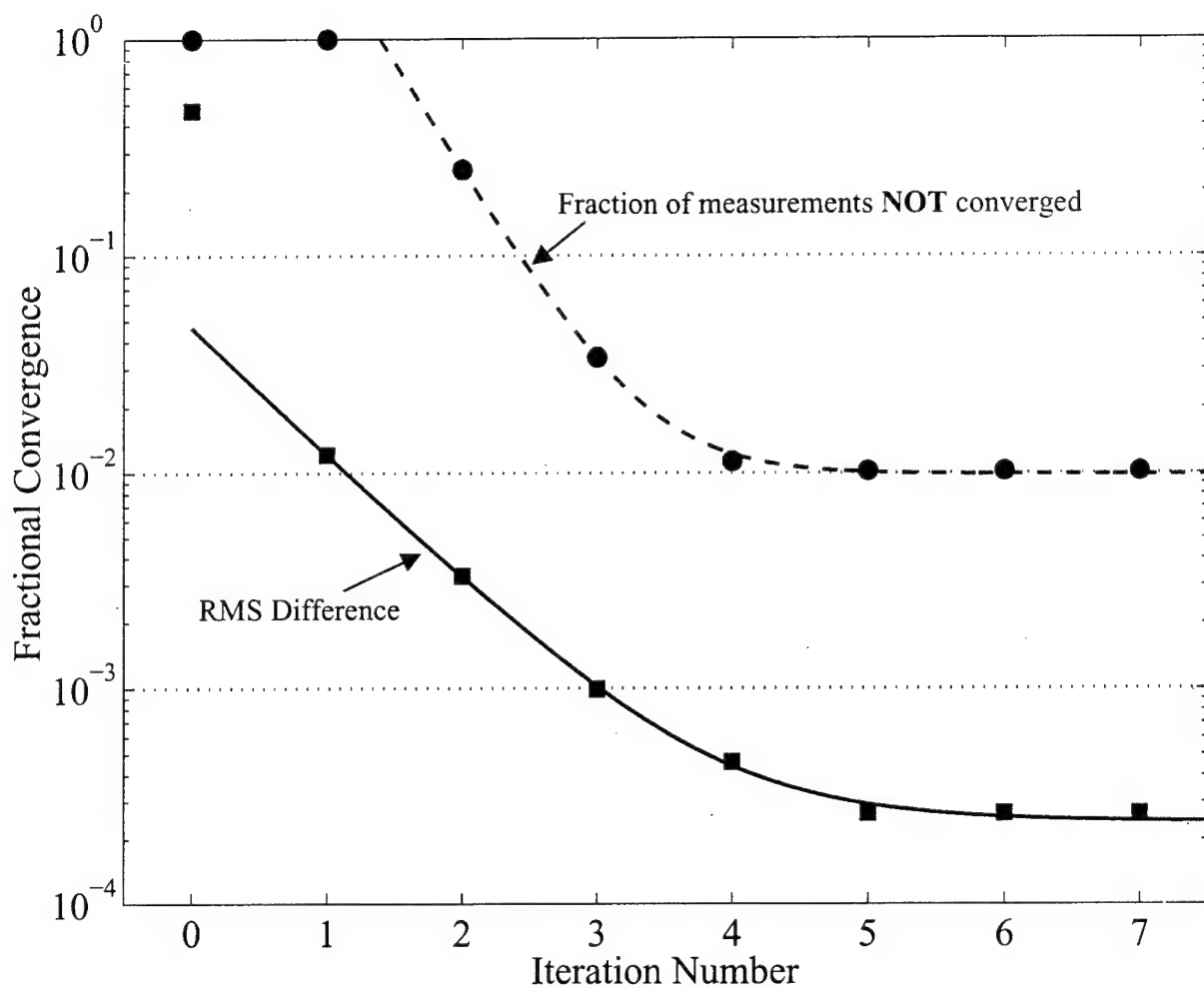
Figure 13. Convergence characteristics of CDI algorithm. The square symbols (■) and the solid curve show the RMS difference between successive iterations normalized by the RMS of the velocity field. The circular symbols (●) and the dashed curve show the fraction of the velocity measurements that have *not* converged as a function of iteration number. Both data sets are modeled quite well by a decaying exponential function.
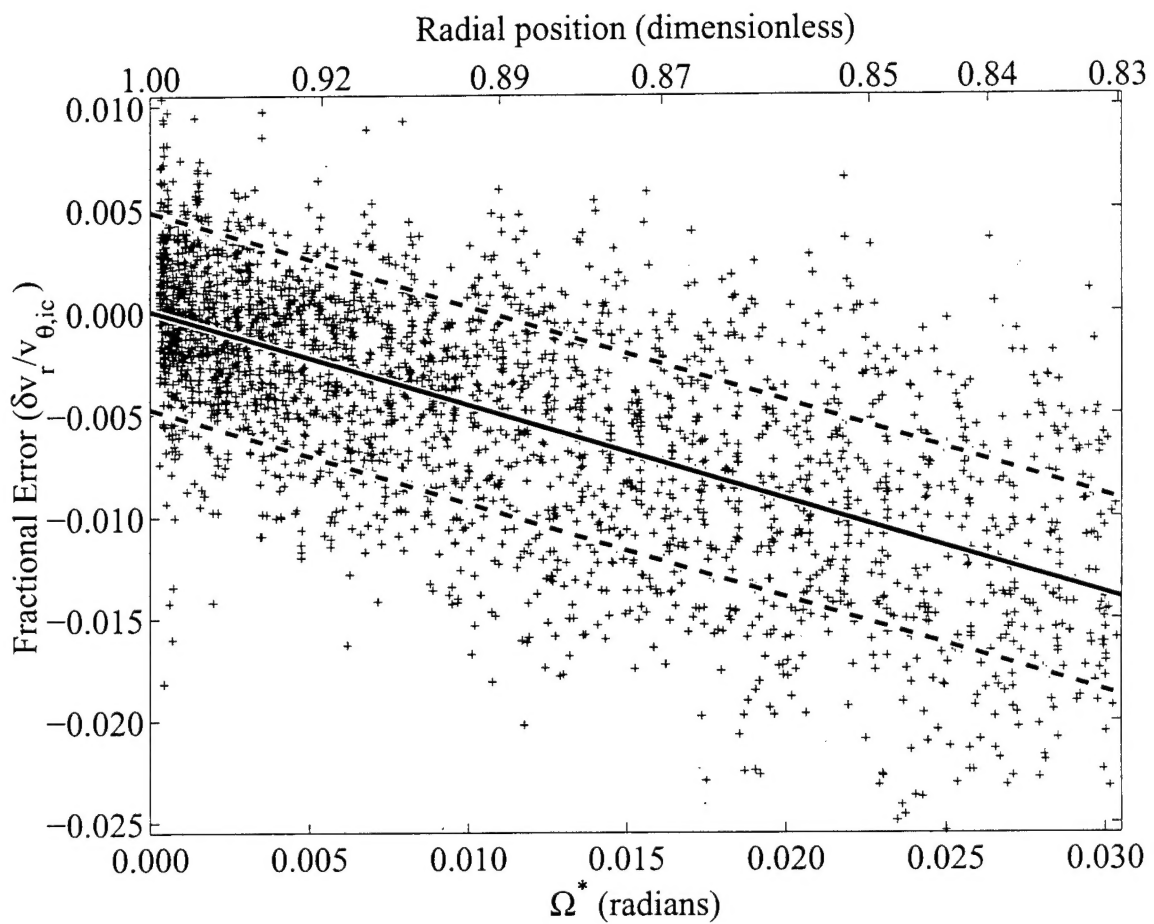
Figure 14. Typical distribution of velocity measurements, each marked by a plus (+) sign, about the predicted bias error curve. The left side of the plot corresponds to stationary outer cylinder while the right side of the figure corresponds to the rotating inner cylinder. The scatter of the points indicates the random error (±0.0048) while the general trend indicates the velocity bias error.
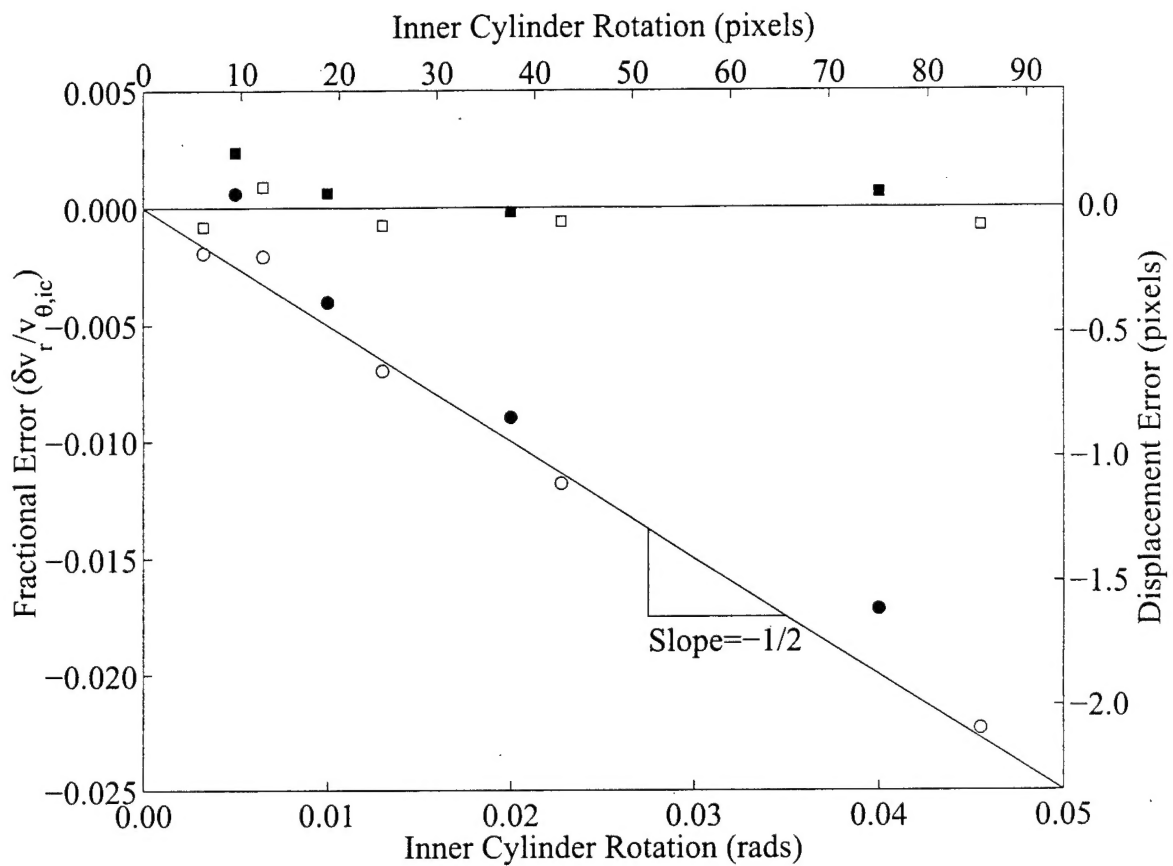
Figure 15. Comparison of the radial velocity errors in the forward difference and central difference discretizations. Square symbols (□,■) represent central difference interrogation while circles (O,●) represent forward difference interrogations. Filled symbols (●,■) represent interrogations of experimental data while the hollow symbols (O,□) represent the Monte Carlo results. The bottom horizontal axis is scaled in radians of rotation of the inner cylinder while the top horizontal axis is scaled in pixels of displacement of the inner cylinder. The left vertical axis is scaled as the fractional velocity error while the right vertical axis is scaled as the displacement error in pixels.
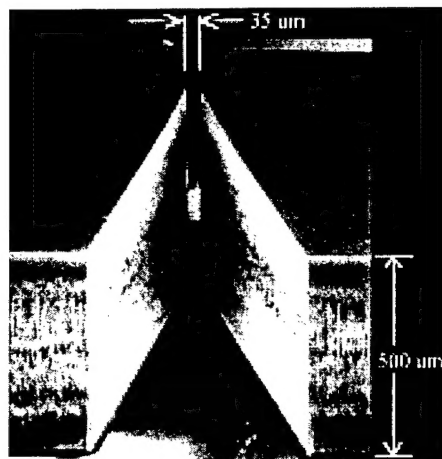
Figure 16. An example of a Silicon-micromachined nozzle. The 2-D nozzle contours are machined into the Silicon using Deep Reactive Ion Etching (DRIE). The top and bottom of the nozzle are formed by anodically bonding two glass wafers to the Silicon wafer. (Photo courtesy Robert Bayt, MIT)
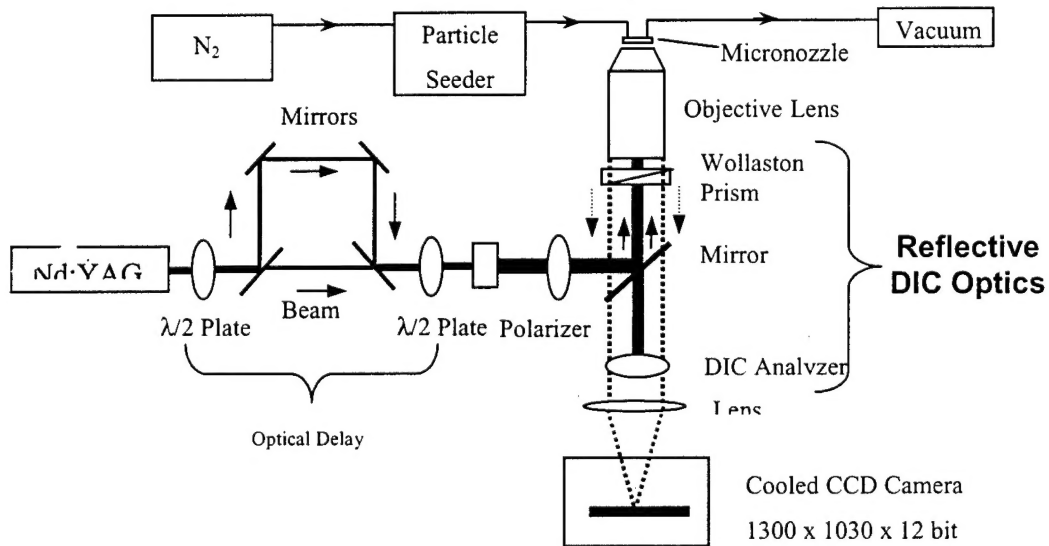

Figure 17. Schematic of a micron-resolution PIV system. The system incorporates a reflective DIC technique to record images of 50 – 100 nm dia. particles. An optical delay path can be added to the system to produce two pulses of laser light separated by tens of nanoseconds.
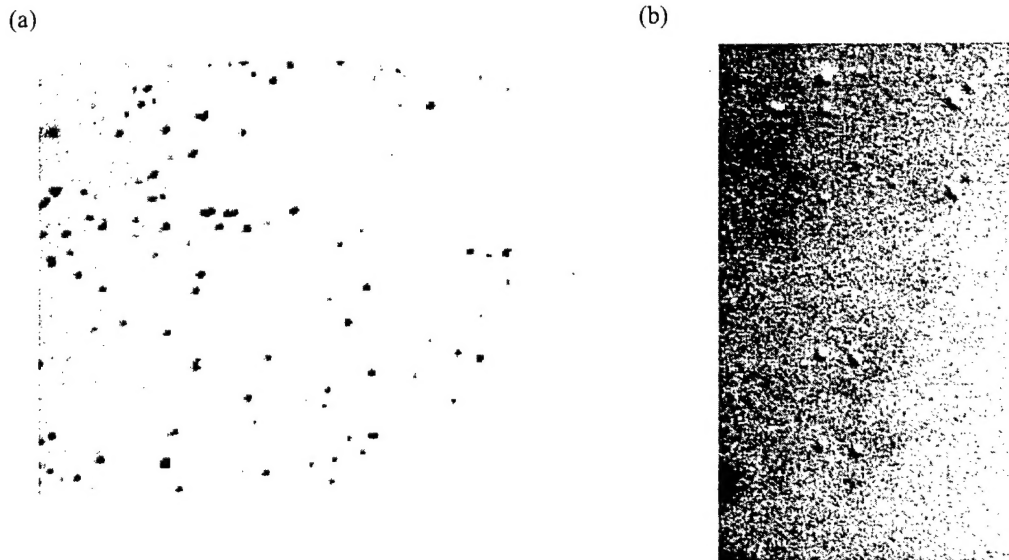
Figure 18. Differential Interference Contrast (DIC) images of 50 nm dia. Silicate particles: (a) recorded using a NA = 1.4 oil immersion 100x objective lens, (b) recorded using a NA = 0.6 air immersion 40x objective lens

Re = 10, 3.4 Y Resolution 96mm/sec →
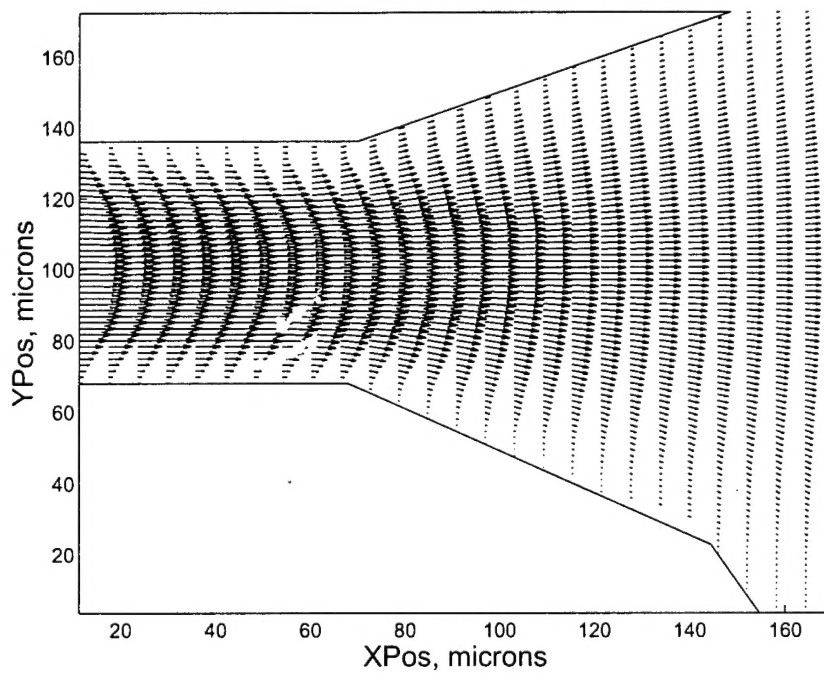
Figure 19. PIV vector field of water flow through a Silicon micromachined nozzle. The nozzle throat is 70 μm wide throat and leads into a constant-angle expansion section. The spatial resolution of the PIV measurements are 10.9×3.4 μm in the streamwise and cross-flow directions, respectively.